#### STRUCTURAL BIOLOGY

# Structural insights into the mechanism of human NPC1L1-mediated cholesterol uptake

Miaoqing Hu<sup>1,2†</sup>, Fan Yang<sup>1†</sup>, Yawen Huang<sup>1†</sup>, Xin You<sup>1</sup>, Desheng Liu<sup>1</sup>, Shan Sun<sup>1</sup>\*, Sen-Fang Sui<sup>1,2</sup>\*

Niemann-Pick C1-like 1 (NPC1L1) protein plays a central role in the intestinal cholesterol absorption and is the target of a drug, ezetimibe, which inhibits NPC1L1 to reduce cholesterol absorption. Here, we present cryo-electron microscopy structures of human NPC1L1 in apo state, cholesterol-enriched state, and ezetimibe-bound state to reveal molecular details of NPC1L1-mediated cholesterol uptake and ezetimibe inhibition. Comparison of these structures reveals that the sterol-sensing domain (SSD) could respond to the cholesterol level alteration by binding different number of cholesterol molecules. Upon increasing cholesterol level, SSD binds more cholesterol molecules, which, in turn, triggers the formation of a stable structural cluster in SSD, while binding of ezetimibe causes the deformation of the SSD and destroys the structural cluster, leading to the inhibition of NPC1L1 function. These results provide insights into mechanisms of NPC1L1 function and ezetimibe action and are of great significance for the development of new cholesterol absorption inhibitors.

Copyright © 2021
The Authors, some rights reserved; exclusive licensee
American Association for the Advancement of Science. No claim to original U.S. Government Works. Distributed under a Creative
Commons Attribution
NonCommercial
License 4.0 (CC BY-NC).

#### INTRODUCTION

Cholesterol is an essential component for cell survival in mammals. As the main constituent of cell membranes, it plays pivotal roles in membrane fluidity, intracellular membrane trafficking and sorting, and cell signaling, and in the body, it is the crude materials for the formation of bile salts and the precursors of steroid hormones (1, 2). The proper regulation of cholesterol levels is critical for human health. High circulation levels of total cholesterol and low-density lipoprotein cholesterol (LDL-C) have been demonstrated to be directly correlated with the risk of atherosclerotic cardiovascular disease (2), which becomes the leading cause of death in developed countries (3). As it is a risk factor for human health, people have made great efforts to find drugs that could reduce the level of plasma cholesterol. Mammals acquire cholesterol mainly from de novo biosynthesis and intestinal absorption (4). The studies of biosynthesis pathway have led to the development of statin drugs that lower LDL-C by inhibiting 3-hydroxy-3-methyl-glutaryl coenzyme A (HMG-CoA) reductase, the rating-limiting enzyme in cholesterol synthesis (5). Further efforts to lower LDL-C led to the discovery of ezetimibe (EZE) that lowers LDL-C by inhibiting cholesterol absorption from the intestines (6–8). Evidences showed that EZE can be used together with any statin, and such coadministration may lead to greater reduction in blood total cholesterol and LDL-C (9). The further search for the key protein(s) of the target of EZE resulted in the discovery of Niemann-Pick C1-like 1 (NPC1L1) (10–12). Subsequent studies confirmed that NPC1L1 plays a key role in both dietary cholesterol adsorption and biliary cholesterol re-adsorption and that it is the target of EZE (11).

NPC1L1 is a 1332-amino acid membrane protein localizing on the brush membrane of the small intestine in mammals and the canalicular membrane of hepatocytes in primates (1, 4). The NPC1L1 sequence shares 42% identity and 51% similarity with that of Niemann-Pick disease type C1 (NPC1) (13), a membrane protein functioning in the late endosome/lysosome. As the homolog of NPC1, NPC1L1 also has three large lumen domains, N-terminal domain (NTD), middle domain (MLD), and cysteine-rich domain (CTD) in the extracellular region, and one transmembrane domain (TMD) containing 13 transmembrane helices (TMs) embedded in the membrane (1).

Among the lumenal domains, NTD has been demonstrated to bind cholesterol directly in vitro (14), and the MLD was reported to have a binding site for the inhibitor EZE (15). The EZE analog, EZE-phosphatidylserine (PS), was detected to bind to the pocket formed by the three extracellular domains of NTD, MLD, and CTD in rat NPC1L1 (16). TM3 to TM7 constitute the sterol-sensing domain (SSD), which is conserved in several cholesterol-related proteins (17), such as NPC1 (18), the sterol regulatory element-binding protein cleavage-activating protein (SCAP) (19), the HMG-CoA reductase (20), Hedgehog receptor Patched (21), and Hedgehog release protein Dispatched (22). The SSD-intervening loops ( $Loop^{TM1-TM2}$ ,  $Loop^{TM3-TM4}$ ,  $Loop^{TM5-TM6}$ , and  $Loop^{TM7-TM8}$ ) and the C-terminal cytoplasmic tail are located on the cytoplasmic side (16). The  ${
m Loop}^{
m TM7-TM8}$  was suggested to be an important element for cholesterol uptake (23), and the C-terminal cytoplasmic tail has been detected to have internalization motif for endocytosis (24). An internal tunnel that connects the extracellular domains to SSD was delineated in the structure of rat NPC1L1 (16) and also suggested in the structures of Niemann-pick C-related protein 1 (NCR1) (25), NPC1 (26), and Patched1 (21). In these structures, similar sterol-like molecules were observed in distinct positions of the tunnel. Thus, the tunnel has been proposed to be the transport path of cholesterol from the NTD to the membrane. However, whether the binding of the sterol-like molecules in the tunnel is directly involved in the transport process and how the SSD interacts with cholesterol are the questions that need to be further clarified.

In the meantime, considerable studies by using biochemical and cellular biological approaches have suggested that NPC1L1-mediated cholesterol uptake is through vesicular endocytosis. A

<sup>&</sup>lt;sup>1</sup>State Key Laboratory of Membrane Biology, Beijing Advanced Innovation Center for Structural Biology, Beijing Frontier Research Center for Biological Structure, School of Life Sciences, Tsinghua University, Beijing 100084, China. <sup>2</sup>Department of Biology, Southern University of Science and Technology, Shenzhen 518055, Guangdong, China.

<sup>\*</sup>Corresponding author. Email: suisf@mail.tsinghua.edu.cn (S.-F.S.); shansun@mail. tsinghua.edu.cn (S.S.)

<sup>†</sup>These authors contributed equally to this work.

clathrin-dependent (27), but not caveolae-mediated, endocytosis (28) was observed. In addition, the interaction of NPC1L1 with lipid raft proteins has been investigated, and EZE may block the formation of cholesterol-enriched microdomains (29). NPC1L1 is located in the endocytic recycling compartment (ERC) when the cholesterol is enriched in cells, while depleting the cholesterol in cells results in the movement of NPC1L1 to the plasma membrane (PM) that is mediated by LIM domain and actin binding 1 (LIMA1) and Myosin Vb (30, 31). However, how the NPC1L1 protein senses the cholesterol level and how the cholesterol level regulates the endocytosis process of NPC1L1 remain to be elucidated.

To address these questions, we resolved four cryo–electron microscopy (cryo-EM) structures of human NPC1L1: the full-length human NPC1L1 in apo form (FL-hNPC1L1-Apo) at a resolution of 3.03 Å, the NTD-truncated hNPC1L1 in apo form ( $\Delta$ N-hNPC1L1-Apo) at 3.14 Å, the  $\Delta$ N-hNPC1L1 in cholesterol-enriched form at 2.69 Å ( $\Delta$ N-hNPC1L1-CLR), and the  $\Delta$ N-hNPC1L1-CLR treated with EZE at 3.37 Å ( $\Delta$ N-hNPC1L1-CLR-EZE). These high-quality structures, in combination with biochemical and cellular experiments, not only provide novel and fundamental insights into the mechanisms of the NPC1L1-mediated cholesterol uptake and EZE action but also are of great significance for the development of new cholesterol absorption inhibitors.

#### **RESULTS**

### Structures of the human NPC1L1 in the apo form

To investigate the mechanism underlying the cholesterol transport mediated by NPC1L1, we first sought to resolve the structure of hNPC1L1 in the apo form. Two constructions were used: One is the full-length hNPC1L1 (FL-hNPC1L1), and the other one is the ΔN-hNPC1L1, in which the N-terminal sequence before the amino acid Ala<sup>265</sup> was deleted given the potential dynamic position of the NTD due to the very long linker of 20 residues (A265 to S284) between the NTD and the TM1 (fig. S1A). The FL-hNPC1L1 (1 to 1332 amino acids) with C-terminal FLAG was expressed in human embryonic kidney (HEK) 293F cells and purified in digitonin for cryo-EM analysis (fig. S1B). We collected 1,918,878 particles for two-dimensional (2D) class average, and no one class was found to show the structural feature of NTD (fig. S1C), indicating its flexible nature. We lastly obtained the 3D structure of the FL-hNPC1L1-Apo from 220,927 selected particles at a resolution of 3.03 Å with no density for the NTD (Fig. 1A and fig. S1, D to G). Apart from the NTD, the overall structure agrees well with the topology predicted from its sequence and biochemical data. It has an approximate dimension of 115 Å by 56 Å by 56 Å and displays two lumenal domains of MLD and CTD and one TMD (TM2 to TM13) (Fig. 1B). It should be mentioned that the recently published structure of the rat NPC1L1 contains the NTD that rotates ~60° from the apo state (FL-rNPC1L1-Apo) to the EZE-PS-bound state (FL-rNPC1L1-EZEPS), consistent with its dynamic nature (16). The difference of the presence of the NTD in the rat NPC1L1 structure and the absence of the NTD in the human NPC1L1 structure may be due to the low-sequence conservation in the region followed by the NTD to the IH1 (fig. S1A). Except for the NTD, FL-hNPC1L1-Apo and FL-rNPC1L1-Apo share high structural conservation with a root mean square deviation (RMSD) of 1.994 Å over the Cα atoms when the two structures are superimposed (fig. S2A), and the MLD, CTD, and TMD can be superimposed to the corresponding domains in

FL-rNPC1L1-Apo with RMSD values of 0.722, 0.907, and 1.761 Å, respectively (fig. S2, B to D).

There are 10 N-glycosylation sites, including N<sub>416</sub>RSS, N<sub>431</sub>FSG, N<sub>464</sub>ISL, N<sub>479</sub>TSL, N<sub>497</sub>RTL, N<sub>506</sub>QTL, N<sub>909</sub>FSS, N<sub>927</sub>FSF, N<sub>1037</sub>LTS, and  $N_{1075}ITA$ , at the lumenal domains revealed by the density map (Fig. 1, A and B, and fig. S3A). We observed a stretched density at the center of the protein (Fig. 1C). In detail, this density is in the cavity surrounded by the MLD and CTD and extended into the neck region, which was defined as the segments that connect the lumenal domains to the TMD and include the neck helix 3 connecting MLD to the following TM3, the neck helix 9 connecting CTD to the following TM9, the linker 2 connecting TM2 and MLD, and the linker 8 connecting TM8 and CTD (Fig. 1D). Because similar densities were also seen in the structures of FL-rNPC1L1-Apo (16) and NPC1 (26) and were modeled as a cholesterol, we first assigned this density as a cholesterol. But unexpectedly, the density was much longer than and not fitted well with the cholesterol (fig. S3B). Instead, this density is better defined and has a size and shape consistent with a n-dodecyl- $\beta$ -D-maltoside (DDM) molecule, which was in the buffer used for the protein extraction (Fig. 1, C and D, and fig. S3B). Thus, we modeled this density as a DDM molecule, although other endogenous molecule for this density could not be excluded. More than 20 hydrophobic residues including 11 residues from the MLD and CTD, 9 residues from the neck region, and 5 residues from TM5, TM7, TM11, and TM13, together contour the binding site for the DDM-like molecule (Fig. 1E). Several potential H-bonds are also formed between the DDM-like molecule and residues Thr<sup>407</sup>, Gln<sup>873</sup>, and Tyr<sup>886</sup> (Fig. 1E).

Similar to NPC1, the TMD has a twofold pseudosymmetry (fig. S3C). SSD (TMs 3 to 7) and TMs 9 to 13 have a similar overall architecture (fig. S3C) and share 15% sequence similarity (fig. S3D), suggesting that TMs 9 to 13 are SSD-like domain (SSDL). In our cryo-EM map, we observed four strong elongated densities at the surface of the TMD, likely corresponding to the endogenous bound sterol molecules. We modeled a cholesterol molecule into each density because cholesterol fits well into these densities (Fig. 1F and fig. S3E). Three of four cholesterol molecules (labeled as CLR-1 to CLR-3) are located on the membrane-facing side of the SSD, and only one cholesterol (labeled as CLR-4) is from the SSDL (Fig. 1B). It is well known that the TMs 3 to 5 form a V-shaped surface cavity usually occupied by sterol molecules (16, 21, 32), which is the notable structural feature of SSD. In our structure, a cholesterol molecule (CLR-1) is seen to bind to this cavity (Fig. 1G). Eleven hydrophobic residues from TMs 2 to 5 and only one hydrophobic residue from the linker 2 surround CLR-1 (Fig. 1H). In particular, Pro<sup>703</sup>, as the conserved residue in the NPC1 (Pro691) (33) and Patched1 (Pro504) (32), directly participates in the cholesterol interaction (Fig. 1H). In addition, the cholesterol also makes two potential hydrogen bonds (H-bonds) with Thr<sup>376</sup> and Glu<sup>374</sup> from the linker 2 (Fig. 1H). Thus, from both the space and the energetics aspect, cholesterol in the V-shaped SSD shelf is at its situation with the most favorable state.

We also expressed and purified  $\Delta N$ -hNPC1L1 in the apo state (fig. S1B). As expected, without the dynamic NTD,  $\Delta N$ -hNPC1L1 exhibited higher stability and higher expression level than FL-hNPC1L1. We lastly determined the structure of the  $\Delta N$ -hNPC1L1-Apo at a resolution of 3.14 Å (fig. S4, A, B, and E). Structural comparison showed no obvious differences between FL-hNPC1L1-Apo and  $\Delta N$ -hNPC1L1-Apo (fig. S4F). Some key features such as the central DDM-like molecule and the cholesterol in the SSD pocket remain

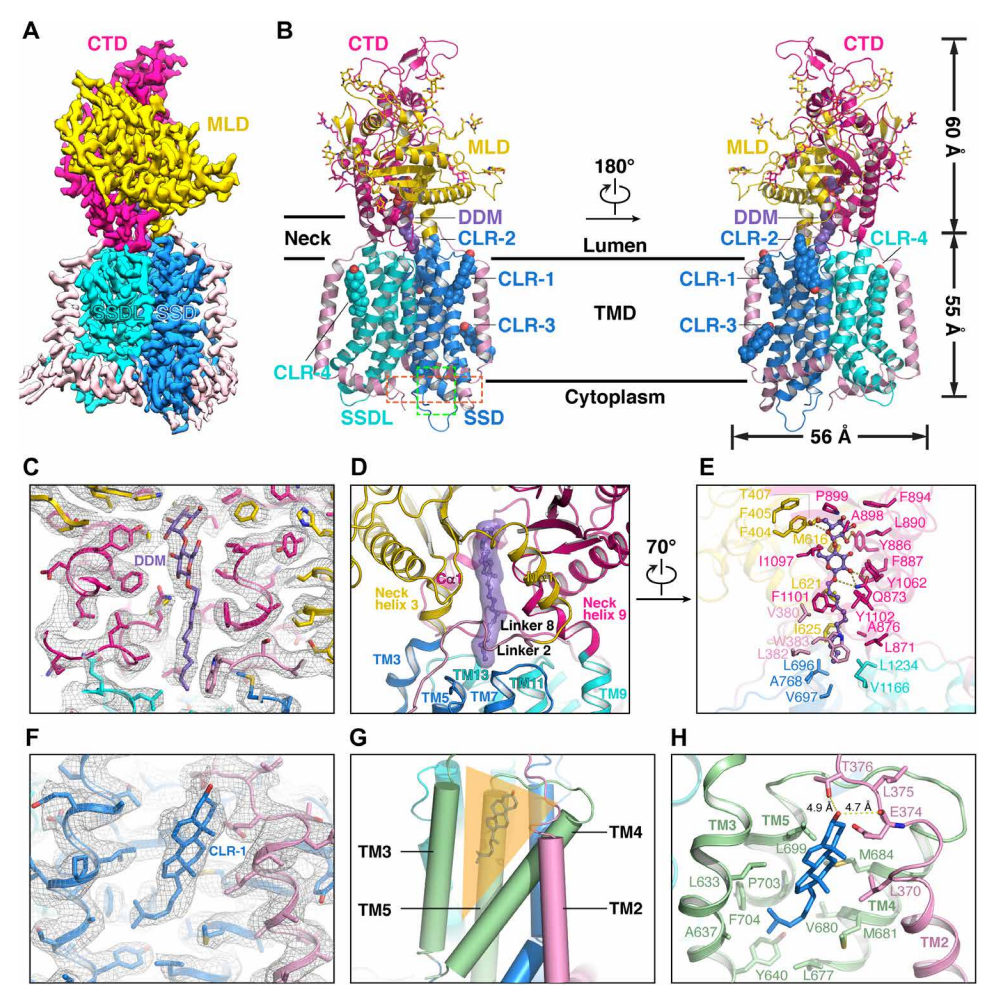


Fig. 1. Structures of the human NPC1L1 in the apo form. (A) Cryo-EM density map of the human NPC1L1 in the apo form (FL-hNPC1L1-Apo) at an overall resolution of 3.03 Å colored by domains. SSDL, SSD-like domain. (B) The overall structure of FL-hNPC1L1-Apo. The cholesterol molecules (CLR-1 to CLR-4) and DDM-like molecule (DDM) are shown as spheres. The sugar moieties are shown as sticks. (C) Cryo-EM densities (mesh) are shown as gray meshes for the DDM-like molecule (stick) and surrounding residues (stick). (D) The DDM-like molecule is found at the interface between MLD and CTD and extends into the neck region. (E) Coordination of the DDM-like molecule. (F) Cryo-EM densities (mesh) are shown as gray meshes for the cholesterol molecule CLR-1 (stick) and surrounding residues (stick). (G) CLR-1 is located in the V-shaped surface cavity formed by TMs 3 to 5 of SSD. (H) Coordination of CLR-1.

nearly identical (fig. S4G), which suggested that, in the apo form, truncation of the NTD does not affect the conformation of the rest structure.

## Structure of the human NPC1L1 in the cholesterolenriched state

Because NPC1L1 mediates the intestinal cholesterol absorption, we next aimed to resolve the structure of hNPC1L1 in the cholesterol-enriched state (hNPC1L1-CLR) by replenishing additional cholesterol molecules during the cell culture and the protein purification procedure as described in Materials and Methods. Preliminary assessment using cryo-EM showed that protein particles prepared with FL-hNPC1L1-CLR were distributed in areas where ice thickness was considered to be thick and not ideal for cryo-EM due to the significantly weak contrast (fig. S4H). In contrast, the protein particles prepared with  $\Delta$ N-hNPC1L1-CLR were homogeneous in the thin layer of vitreous ice. We therefore focused on the  $\Delta$ N-hNPC1L1-CLR for the cryo-EM analysis. Both monomer and dimer were

observed during the data processing, but we could not refine the structure of dimer because of the limited number of particles. Last, we obtained the structure of the monomeric  $\Delta N$ -hNPC1L1-CLR at a resolution of 2.69 Å (Fig. 2A and fig. S4, A, C, and D).

Structural comparison between  $\Delta N$ -hNPC1L1-CLR and  $\Delta N$ -hNPC1L1-Apo showed the similarity in the extracellular region (Fig. 2B). The DDM-like molecule lies in the same position of the central cavity (fig. S5A). In the TMDs, however,  $\Delta N$ -hNPC1L1-CLR exhibits obvious differences, particularly in the SSD region, which has two distinct structural features (Fig. 2B). First, two more cholesterol molecules (CLR-5 and CLR-6) were observed to bind to the SSD in the cholesterol-enriched structure, except that the three original ones (CLR-1 to CLR-3) in the apo structure are still there with the same orientations (Fig. 2B). The second structural feature of SSD in  $\Delta N$ -hNPC1L1-CLR is found around the connection region of Loop 3-4 (the loop connecting TM3 and TM4, G652-T667) and Loop 7-8 (the loop connecting TM7 and IH2, R801-L828), where the newly bound cholesterol molecule, CLR-6, interacts with

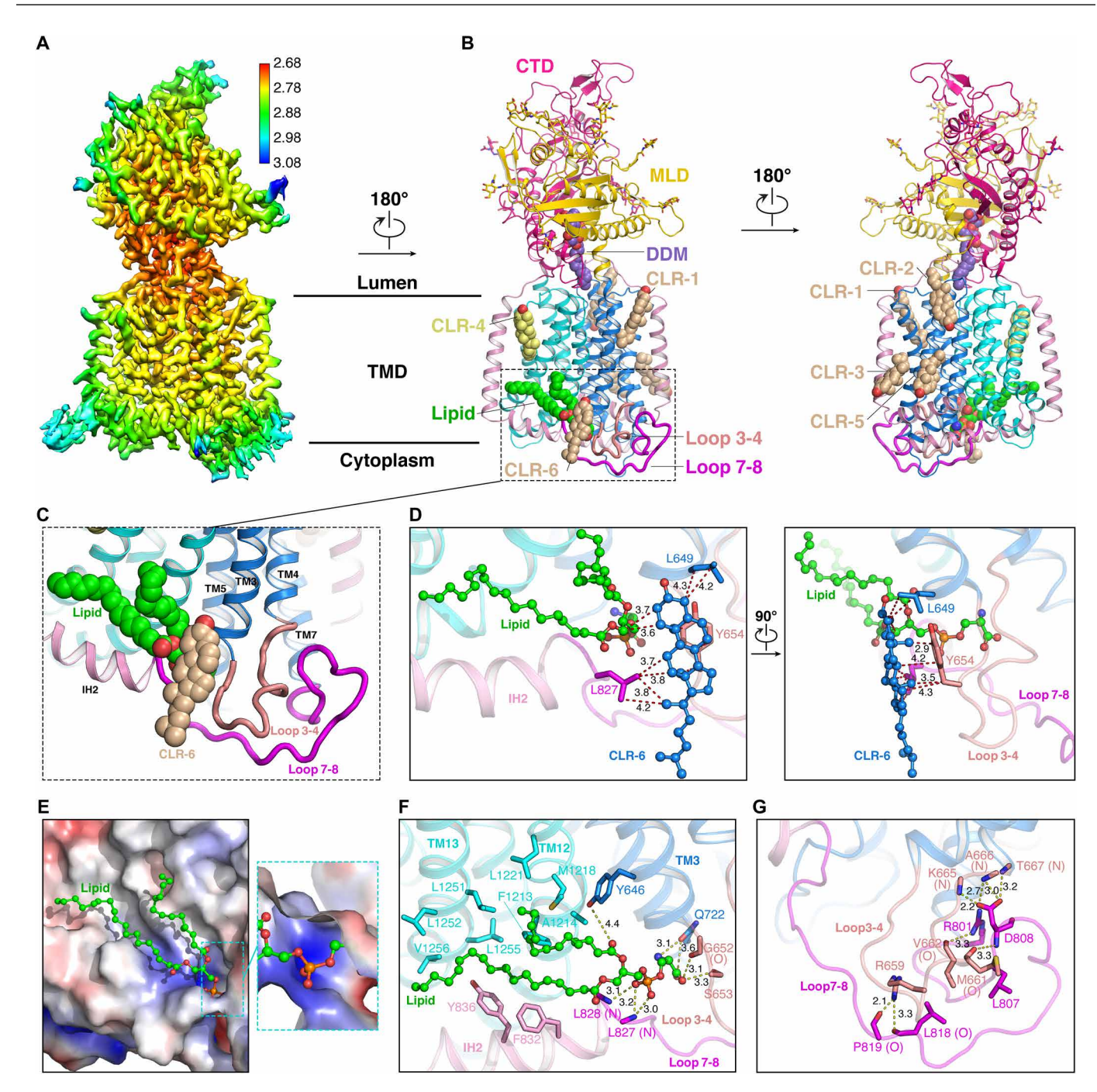


Fig. 2. Structure of the human NPC1L1 in the cholesterol-enriched state. (A) Cryo-EM density map of the NTD-truncated human NPC1L1 in the cholesterol-enriched form (ΔN-hNPC1L1-CLR) at an overall resolution of 2.69 Å colored by local resolutions. The local resolutions were calculated in RELION. (B) The overall structure of ΔN-hNPC1L1-CLR. The cholesterol molecules (CLR-1 to CLR-6), the PS-like lipid (lipid), and the DDM-like molecule (DDM) are shown as spheres. The sugar moieties are shown as sticks. The structural cluster is boxed by black dashed line and enlarged in (C). (C) The structural cluster is formed by four elements: the cholesterol molecule CLR-6, the PS-like lipid, and Loops 3-4 and 7-8. (D) The interactions of CLR-6 with the PS-like lipid, and Loops 3-4 and 7-8 from two perpendicular views. (E) The two hydrophobic tails of the PS-like lipid are bound to the hydrophobic surface, and its hydrophilic head inserts into a positively charged pocket. (F) The interactions of the PS-like lipid with the protein. (G) The interactions between Loops 3-4 and 7-8.

Loop 3-4, Loop 7-8, and a lipid-like molecule to form a stable structural cluster of SSD (Fig. 2B and fig. S5).

In the high-quality map of  $\Delta N$  -hNPC1L1-CLR, the SSD-bound CLR-6 is clearly resolved near the Loops 3-4 and 7-8 (Fig. 2C and

fig. S5, B and C). A cholesterol-binding motif named cholesterol recognition amino acid consensus (CRAC), which is generally referred as  $[L/V-X_{1-5}-(Y)-X_{1-5}-K/R]$  in the scientific literature (34), lies at the N-terminal region of Loop 3-4 and has the following

sequence: (649)LALGSYSWSR(659) (amino acid residues that fulfill the CRAC algorithm are in bold and underlined). Here, the amino acid residues involved in cholesterol binding are L649, Y654, and L827, which include the central tyrosine and mandatory leucine in the CRAC motif. As was shown in Fig. 2D, the phenyl ring of the aromatic residue Tyr<sup>654</sup> stacks onto the aliphatic rings of the cholesterol to form the CH- $\pi$  interaction, and it seems that it contributed most energy of the interaction between Loop 3-4 and CLR-6.

In addition to CLR-6, an extra lipid-like density was observed to be located close to the N-terminal region of Loop 3-4 and the C-terminal region of Loop 7-8 (Fig. 2C and fig. S5D). The discernible densities enabled the modeling of one PS-like lipid molecule (fig. S5D). The two hydrophobic tails of this lipid are bound to the hydrophobic surface mostly contributed by a number of hydrophobic residues from TMs 12 and 13 of SSDL, as well as two and one hydrophobic residues from IH2 and TM3, respectively (Fig. 2, E and F). The hydrophilic head inserts into a positively charged pocket comprised the N-terminal ends of Loop 3-4 and Loop 5-6 and the C-terminal end of Loop 7-8 (Fig. 2, E and F). Within this pocket, the polar head of the PS-like lipid is coordinated by the side groups of Ser<sup>653</sup> and Gln<sup>722</sup>, as well as the main chain C=O of Gly<sup>652</sup> and amide groups of Leu<sup>827</sup> and Leu<sup>828</sup> (Fig. 2F). Besides, the PS-like lipid is in close contact with the CLR-6 via hydrophobic interaction (Fig. 2D).

Loops (fig. S5, E and F). As expected, these two loops stretch out from the TMD and extend into the cytosol (Fig. 2, B and C). They are arranged antiparallelly and make extensive polar interactions with each other (Fig. 2, C and G). At the N-terminal region of Loop 7-8, the guanidinium group of Arg<sup>801</sup> engages in a H-bond with the main chain carbonyl oxygen (C=O) of Val<sup>662</sup> in Loop 3-4 (Fig. 2G). Subsequently, the side group of Asp<sup>808</sup> interacts with the main chain amide groups of Lys<sup>665</sup>, Ala<sup>666</sup>, and Thr<sup>667</sup> in Loop 3-4 (Fig. 2G). Moreover, the main chain amide group of Asp<sup>808</sup> forms a H-bond with the main chain C=O of M661 in Loop 3-4 (Fig. 2G). At the C-terminal region of Loop 7-8, the C=O groups of Leu<sup>818</sup> and Pro<sup>819</sup> are coordinated by the side group of Arg<sup>659</sup> in Loop 3-4 (Fig. 2G). Thus, both the side chains and the backbone polar groups participate in the interaction between Loop 3-4 and Loop 7-8. In addition, at the middle of these two loops, four residues, Met<sup>661</sup> and Val<sup>662</sup> in Loop 3-4 and Leu<sup>807</sup> and Leu<sup>818</sup> in Loop 7-8, form a hydrophobic cluster, which also contributes to the interaction (Fig. 2G).

Therefore, the extensive interactions among the four elements, the cholesterol CLR-6, the PS-like lipid molecule, and Loops 3-4 and 7-8 of the protein, stabilize the formation of the structural cluster under the cholesterol-enriched condition.

#### Structure of the human NPC1L1 in the EZE-bound state

To investigate the mechanism of EZE inhibition, we prepared a cryo-EM sample by incubating NPC1L1 in cholesterol-enriched state with EZE in vitro, namely,  $\Delta$ N-hNPC1L1-CLR-EZE, and resolved the structure at a resolution of 3.37 Å by cryo-EM (fig. S6). An extra density was observed at the bottom of the central cavity near to the neck region, allowing us to model the EZE molecule according to the shape and size (Fig. 3, A and B). The binding cavity is mainly contoured by 21 hydrophobic residues from the neck helices, linker 2 and linker 8, and TM5, TM7, TM11, and TM13 (Fig. 3C), which resembles the binding site of the DDM-like molecule in the  $\Delta$ N-hNPC1L1-Apo that is also including the hydrophobic residues from the neck region and TM5, TM7, TM11, and TM13. These two

molecules are lined along the central hole spanning from the lumenal domains to TMD (Fig. 3D). In detail, the DDM-like molecule occupies the top and middle segments of the hole constituted by the MLD-CTD interface and the neck region, respectively, while EZE resides the neck region and the bottom of the hole that is down into the TMD. It is obvious that the DDM-like molecule and EZE clash at the neck region (Fig. 3D and fig. S7A), suggesting a competitive binding between them. Except for the van der Waals contacts of EZE with the surrounding hydrophobic residues, several aromatic residues make  $\pi$ - $\pi$  interactions with EZE (Fig. 3C). Phe<sup>1101</sup> and Tyr<sup>1102</sup> formed one parallel-displaced  $\pi$ - $\pi$  and one T-shaped  $\pi$ - $\pi$  interaction with the phenyl ring 1 of EZE, respectively (Fig. 3C). The phenyl ring 2 is subjected to a T-shaped  $\pi$ - $\pi$  interaction with Phe<sup>1238</sup> (Fig. 3C). Phe<sup>772</sup> and Phe<sup>1239</sup> make two T-shaped  $\pi$ - $\pi$  interactions with the phenyl ring 3. Two potential H-bonds are also formed between EZE and the side group of Gln873 as well as the C-O of Leu<sup>877</sup> (Fig. 3C). To validate the structural observations, we generated three hNPC1L1 mutants designed to disrupt EZE binding (Q873A, F1101A-Y1102A, and F1239R), all of which displayed a pronounced defect in the EZE binding (Fig. 3E).

Similar to the  $\Delta$ N-hNPC1L1-Apo, a cholesterol-like density is also located in the V-shaped SSD shelf of  $\Delta$ N-hNPC1L1-CLR-EZE (Fig. 3F). However, the position and orientation of the cholesterol-like molecule have considerable changes due to the EZE-induced deformation of the SSD shelf, which will be shown in the following section. The hydroxyphenyl group is inserted into the cavity, while the aliphatic chain protrudes toward the extracellular space (Fig. 3F). Eight hydrophobic residues from TMs 2 to 5 and three from the linker 2 participate in the binding of this cholesterol (Fig. 3F).

# Conformational changes of the $\Delta N$ -hNPC1L1 upon binding of EZE

One of the remarkable differences between the structures of FLhNPC1L1-Apo, ΔN-hNPC1L1-CLR, and ΔN-hNPC1L1-CLR-EZE is the presence of the structural cluster formed by CLR-6, the PS-like lipid, and Loops 3-4 and 7-8 in the SSD in the  $\Delta$ N-hNPC1L1-CLR (Fig. 4A), but this cluster is invisible in FL-hNPC1L1-Apo and  $\Delta$ NhNPC1L1-CLR-EZE (Fig. 4A). Apart from these loops and lipids, FL-hNPC1L1-Apo is nearly identical to the ΔN-hNPC1L1-CLR with the RMSD of 0.445 Å over 918 Cα atoms (fig. S7B). However, the RMSD between ΔN-hNPC1L1-CLR and ΔN-hNPC1L1-CLR-EZE rises to 1.091 Å over 897 Cα atoms (fig. S7C), suggesting that there are pronounced structural differences between ΔN-hNPC1L1-CLR and ΔN-hNPC1L1-CLR-EZE. Individual domain comparison shows that the two lumenal domains remain nearly unchanged with the RMSD of 0.794 Å (fig. S7D), while the RMSD between the TMDs increases to 1.203 Å over only 313 Cα atoms (fig. S7E). Further comparison using the lumenal domains as the alignment reference shows that SSDL is relatively stable with the RMSD of 1.552 Å (fig. S7F), while conformational changes of SSD are evident with the RMSD increasing to 2.011 Å (Fig. 4, A and B). The concerted motions of SSD segments upon EZE binding were observed. The penetration of the phenyl ring 3 of EZE into the TMD causes steric clashes with the residues Val<sup>697</sup> on TM5 and Ala<sup>768</sup> on TM7, thus pushing them outward to overcome the steric hindrance (Fig. 4C). The C $\alpha$  atoms of Val<sup>697</sup> and Ala<sup>768</sup> move 2.8 and 0.9 Å, respectively (Fig. 4C). Such conformational shifts further induce the movement of the ensuing TM5 and TM7 accordingly (Fig. 4B). Structural

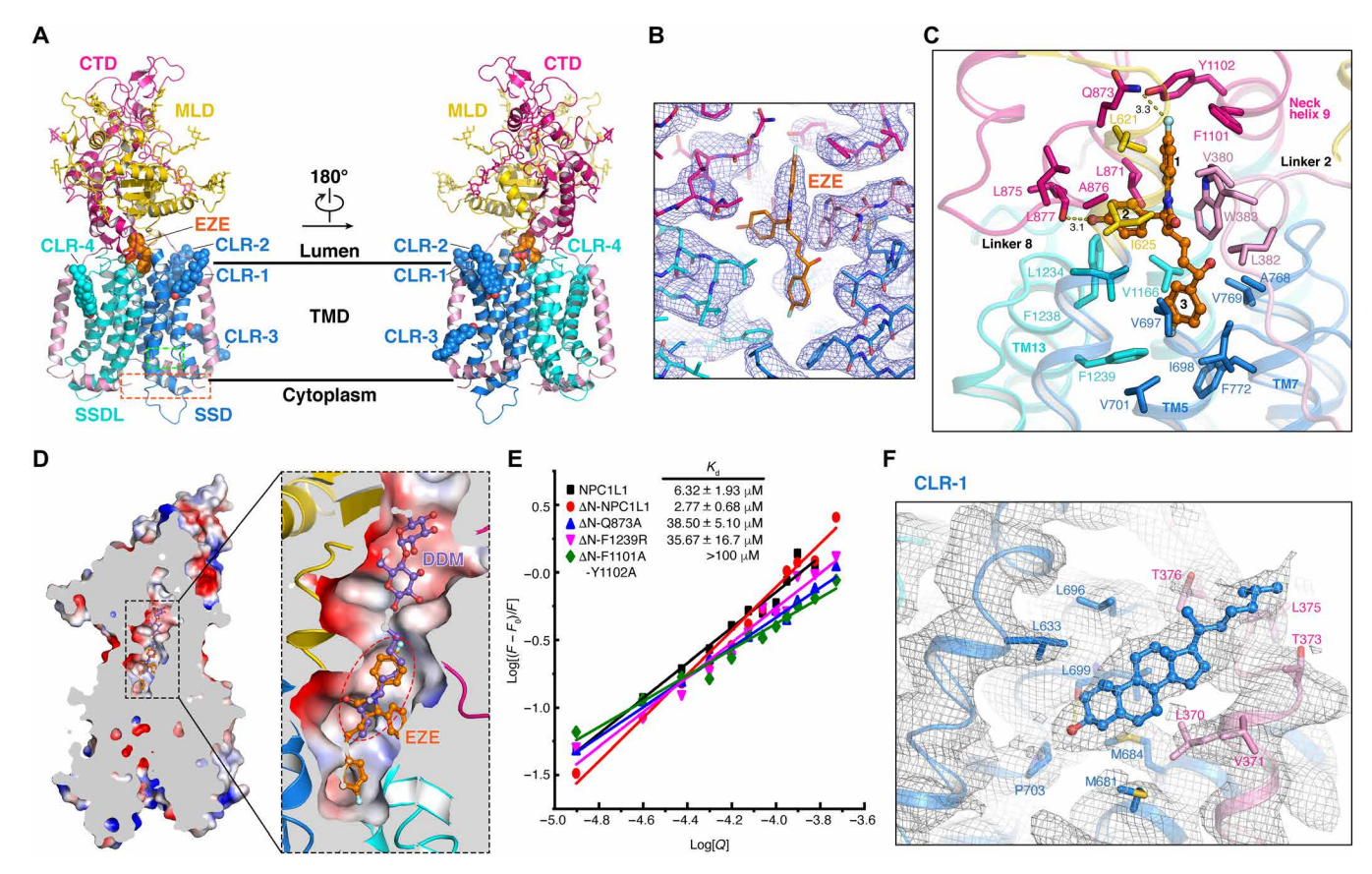


Fig. 3. Structure of the human NPC1L1 in the EZE-bound state. (A) The overall structure of the NTD-truncated human NPC1L1 in the cholesterol-enriched state incubated with EZE (ΔN-hNPC1L1-CLR-EZE). The cholesterol molecules (CLR-1 to CLR-4) and the ezetimibe molecule (EZE) are shown as spheres. The sugar moieties are shown as sticks. (B) Cryo-EM densities (mesh) are shown as blue meshes for the EZE molecule (stick) and surrounding residues (stick). (C) Coordination of EZE. (D) EZE and the DDM-like molecule are lined along the central hole of the NPC1L1 and clash with each other. (E) The dissociation constant (K<sub>d</sub>) values for the wild-type and mutated NPC1L1. (F) Coordination of CLR-1 in the V-shaped surface cavity of SSD.

analysis showed that extensive hydrophobic interactions exist between TM5 and other TMs in SSD, and among each TM in SSD as well as the preceding IH1 (fig. S7G). Because of these tight connections, shifts of TM5 and TM7 are immediately translated to other TMs of SSD and IH1. As a result, each TM in SSD and IH1 undergo concerted shifts, and the extent of the shifts increases gradually from the luminal side to the cytosol side of the TMs (Fig. 4B). The displacement of the TM3 and TM5 from  $\Delta N$ -hNPC1L1-CLR to ΔN-hNPC1L1-CLR-EZE causes two residues, Tyr<sup>646</sup> and Gln<sup>722</sup>, which interact with the PS-like lipid, to move away from the PS-like molecule (Fig. 4D). The distances between them and the PS-like molecule increase from 4.4 Å (with Tyr<sup>646</sup>) and 3.1 Å and 3.6 Å (with Gln<sup>722</sup>) in ΔN-hNPC1L1-CLR to 6.8 Å (with Tyr<sup>646</sup>) and 6.0 Å and 6.4 Å (with Gln<sup>722</sup>) in ΔN-hNPC1L1-CLR-EZE (Fig. 4D). At these long distances, the interactions between PS-like lipid and the protein disappear, which, in turn, destabilizes the PS-like lipid and the nearby cholesterol and loops. This explains the lack of the densities of CLR-6, PS-like lipid, and Loop 3-4 and Loop 7-8 in the ΔN-hNPC1L1-CLR-EZE map. Thus, binding with EZE inhibits the formation of the structural cluster.

As mentioned above, a cholesterol molecule, CLR-1, is observed in the V-shaped SSD cavity of both  $\Delta$ N-hNPC1L1-CLR and  $\Delta$ N-hNPC1L1-CLR-EZE (Fig. 4E). However, the conformation and the

microenvironment of this cholesterol are different between these two structures (Fig. 4E). As was shown in the Fig. 4E, EZE binding causes the movement of TM3, which leads to the overlap of the side chain of Tyr<sup>640</sup> with the CLR-1 in the  $\Delta N$ -hNPC1L1-CLR-EZE (Fig. 4E). Thus, the side chain of Tyr<sup>640</sup> in  $\Delta N$ -hNPC1L1-CLR-EZE turns upward about  $80^{\circ}$ , leading to the smaller shelf of SSD and limited space to hold one cholesterol (Fig. 4E). Therefore, the tail of CLR-1 in  $\Delta N$ -hNPC1L1-CLR-EZE is completely exposed, and its orientation is apparently opposite to that in  $\Delta N$ -NPC1L1-CLR (Figs. 3F and 4E).

# Structural cluster of SSD is important for the NPC1L1-mediated cellular cholesterol uptake

Our structures show that the cholesterol molecule could trigger the formation of the structural cluster composed of CLR-6, PS-like molecule, and Loops 3-4 and 7-8, while binding with EZE would disrupt this cluster. Because EZE is a clinical drug used to reduce intestinal cholesterol absorption by targeting NPC1L1 (35), it is thereby reasonable to postulate that the SSD structural cluster is critical for the cellular cholesterol uptake mediated by the human NPC1L1. To test this hypothesis, we generated NPC1L1 variants, in which some residues involved in the interactions within the cluster were mutated, including L649R, L649R-Y654A, G652A-S653A, and

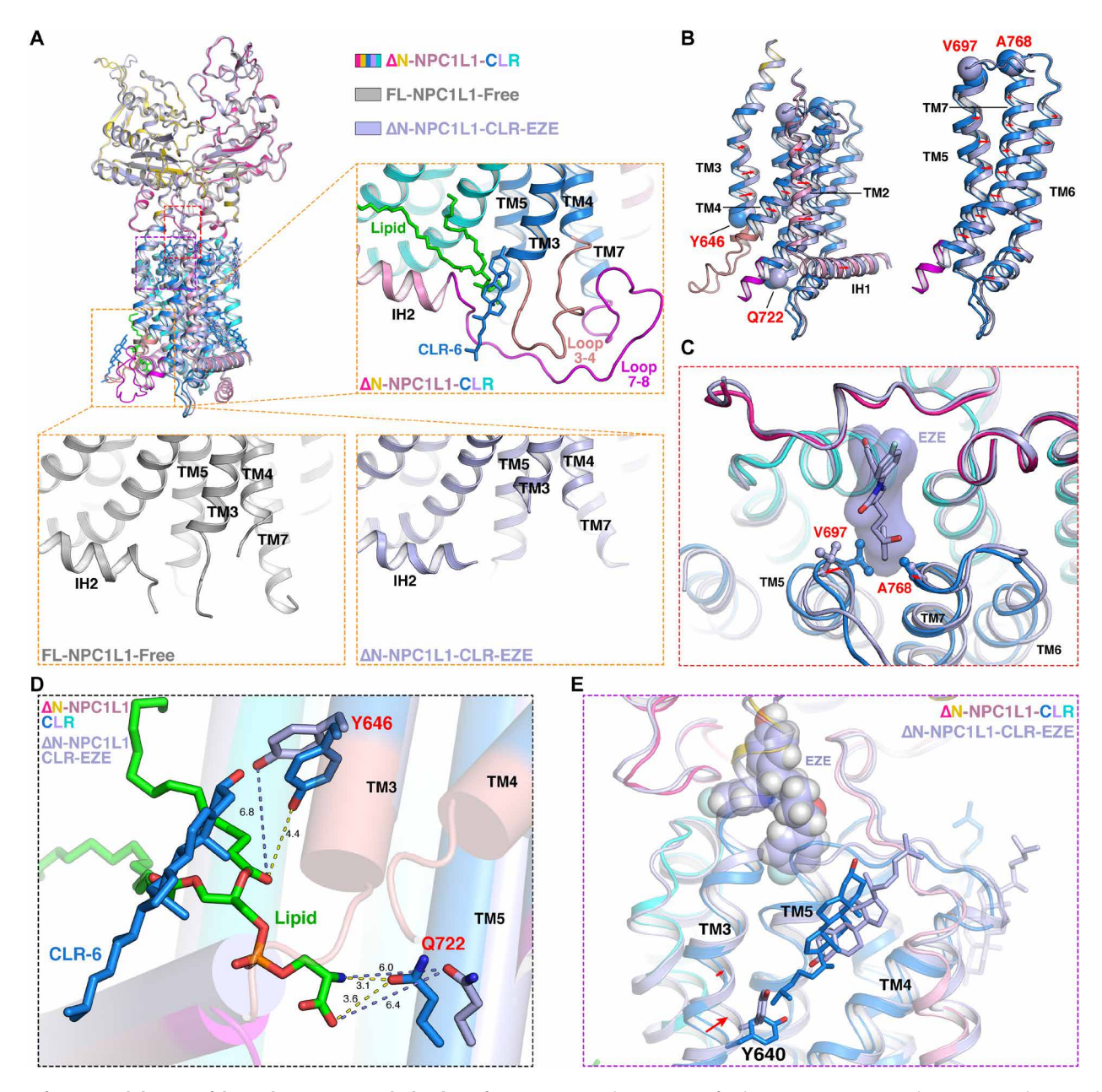


Fig. 4. Conformational changes of the ΔN-hNPC1L1 upon the binding of EZE. (A) Structural comparison of FL-hNPC1L1-Apo (gray), ΔN-hNPC1L1-CLR (domain-colored), and ΔN-hNPC1L1-CLR-EZE (light blue) using the lumenal domains as the alignment reference. Insets show that the structural cluster of SSD is present in the ΔN-hNPC1L1-CLR (upper) but invisible in both FL-hNPC1L1-Apo (middle) and ΔN-hNPC1L1-CLR-EZE (lower). (B) Structural shifts of TMs 1 to 4 and IH1 (left) and TMs 5 to 7 (right) of SSD (red arrows). The key amino acid residues involved in the shifts are shown as spheres. (C) Superimposition of ΔN-hNPC1L1-CLR (domain-colored) and ΔN-hNPC1L1-CLR-EZE (light blue) relative to the lumenal domains shows the clashes between EZE (surface representation superimposed with the atomic model) and the residues (ball-and-stick) V697 on TM5 and A768 on TM7, which push them outward to overcome the steric hindrance (red arrows). (D) The shifts of Y646 and Q722 result in the longer distances between the PS-like molecule and the residues. (E) Structural comparison of the V-shaped SSD pocket in ΔN-hNPC1L1-CLR (domain-colored) and ΔN-hNPC1L1-CLR-EZE (light blue).

L827F-L828A (Fig. 5A). We also generated several deletion mutants, in which parts of Loop 3-4 or Loop 7-8 were deleted (Fig. 5A). Expression plasmids of the wild-type hNPC1L1 or mutants were transiently transfected into CRL1601 cells. The cholesterol uptake was analyzed by filipin staining (31), and the NPC1L1 trafficking was detected by fluorescent imaging (31, 36).

As was shown in the Fig. 5C, after 120 min of cholesterol replenishment, transient expression of wild-type NPC1L1 significantly increased the cellular cholesterol uptake compared with the control cells (nontransfected cells). However, the NPC1L1 mutants only exhibited less than 50% of cholesterol uptake of the wild-type NPC1L1, which suggested that the SSD structural cluster is critical for the

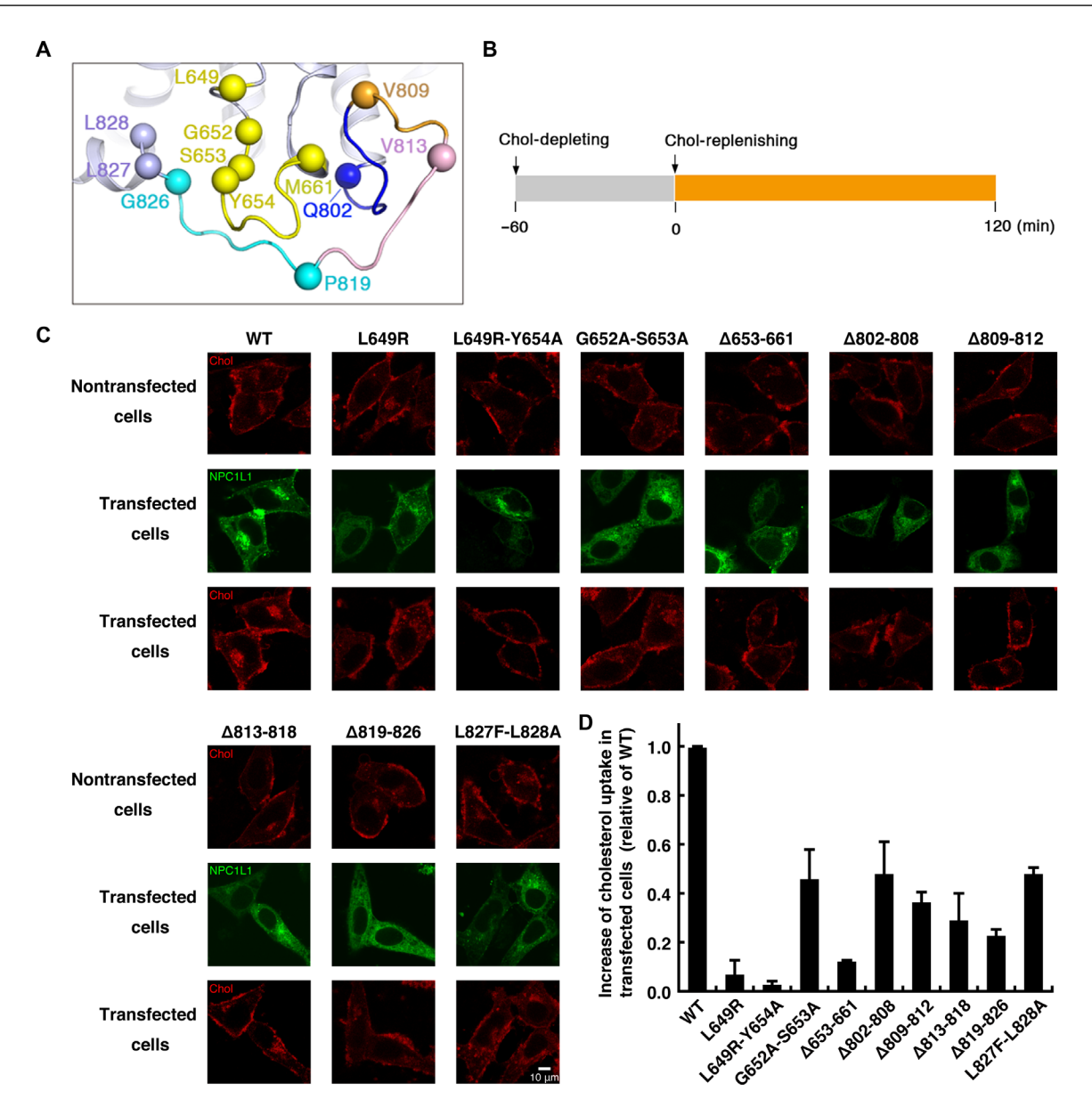


Fig. 5. Cellular cholesterol uptake mediated by the wild-type and mutated human NPC1L1. (A) Diagram showing the positions where hNPC1L1 were mutated or truncated. (B) Diagram showing the procedure used to treat cells. At 36 hours after transfection (–60 min), cells were changed into a cholesterol-depleting medium for 60 min to deplete the cholesterol in the cells (0 min) and then incubated with cholesterol-replenishing medium for another 120 min to deliver cholesterol (120 min). (C) Cells transfected with wild-type (WT) or various mutated hNPC1L1 plasmids were imaged with confocal microscopy at time point 0 min. Scale bar, 10 μm. (D) Fluorescence quantification of cellular cholesterol uptake mediated by hNPC1L1 in (C). The increase of the cholesterol uptake in wild-type hNPC1L1-transfected cells was arbitrarily defined as 1, against which the increase of the cholesterol uptake in mutant hNPC1L1-transfected cells was normalized. Error bars represent standard deviation (SD).

cellular cholesterol uptake mediated by the human NPC1L1. Among these mutants, L649R and L649R-Y654A, in which the residue substitution may interfere with CLR-6 binding, exhibited to be the most severely defective in the cholesterol absorption (7 and 3% of wild-type NPC1L1, respectively) (Fig. 5, C and D), indicating the essentiality of CLR-6 in the structural cluster for the proper function of NPC1L1.

As maturation is the basis for the protein to exert function, and mature NPC1L1 is glycosylated and transported from endoplasmic reticulum (ER) to Golgi, we then examined the glycosylation status of wild-type and mutant NPC1L1 proteins by endoglycosidase H

(Endo H) treatment, which could cleave the ER-resident glycosylated proteins, but not the mature glycosylated proteins, into the unglycosylated forms. As was shown in Fig. 6, ~60% of the wild-type protein was resistant to Endo H digestion, indicating that most of the wild-type protein was in mature glycosylated forms. Most mutant NPC1L1 proteins showed a moderately reduced level of mature glycosylated forms (~30 to 50% of the total protein) compared with the wild-type NPC1L1, and two mutants, L649R-Y654A and  $\Delta$ 809-812, exhibited a slight severe decrease of the mature glycosylated protein (~20% of the total protein). However, the effects of the nine mutations on the protein maturation (represented by the mature

glycosylated protein of mutant NPC1L1 normalized to that of wild-type NPC1L1) were less than those on the cholesterol absorption to different extents (Figs. 5D and 6B). These results suggest that, in addition to the defects in the protein maturation, other factors may also contribute to the impairment of the cholesterol uptake caused by the NPC1L1 mutations in the SSD cluster.

Previous studies have proposed that NPC1L1 mediates cholesterol uptake through its recycle between ERC and PM (30, 31). Cholesterol depletion induces the transport of NPC1L1 from ERC to PM, while cholesterol replenishment leads to the internalization of NPC1L1 (30, 31). Because our data demonstrated that the NPC1L1 mutants of the SSD cluster impaired the cholesterol uptake, we then

tested whether these mutants were defective in the cholesterol-regulated trafficking. At the –60-min point, wild-type NPC1L1 was mainly localized at the perinuclear compartment area of the cells. After depleting cellular cholesterol for 60 min, about ~50% of the total NPC1L1 moved to PM (Fig. 7, A and B). Then, most of the PM-localized NPC1L1 (72%) were internalized after the cholesterol replenishment (Fig. 7, A and C). However, NPC1L1 mutants showed different cellular distribution in responding to cellular cholesterol alterations. After depleting cellular cholesterol, the protein fraction of NPC1L1 mutants moving to PM was reduced to only ~10 to 30% of the total protein (Fig. 7, A and B). Among these mutants, the mutants related to CLR-6 binding (L649R, L649R-Y654A, and

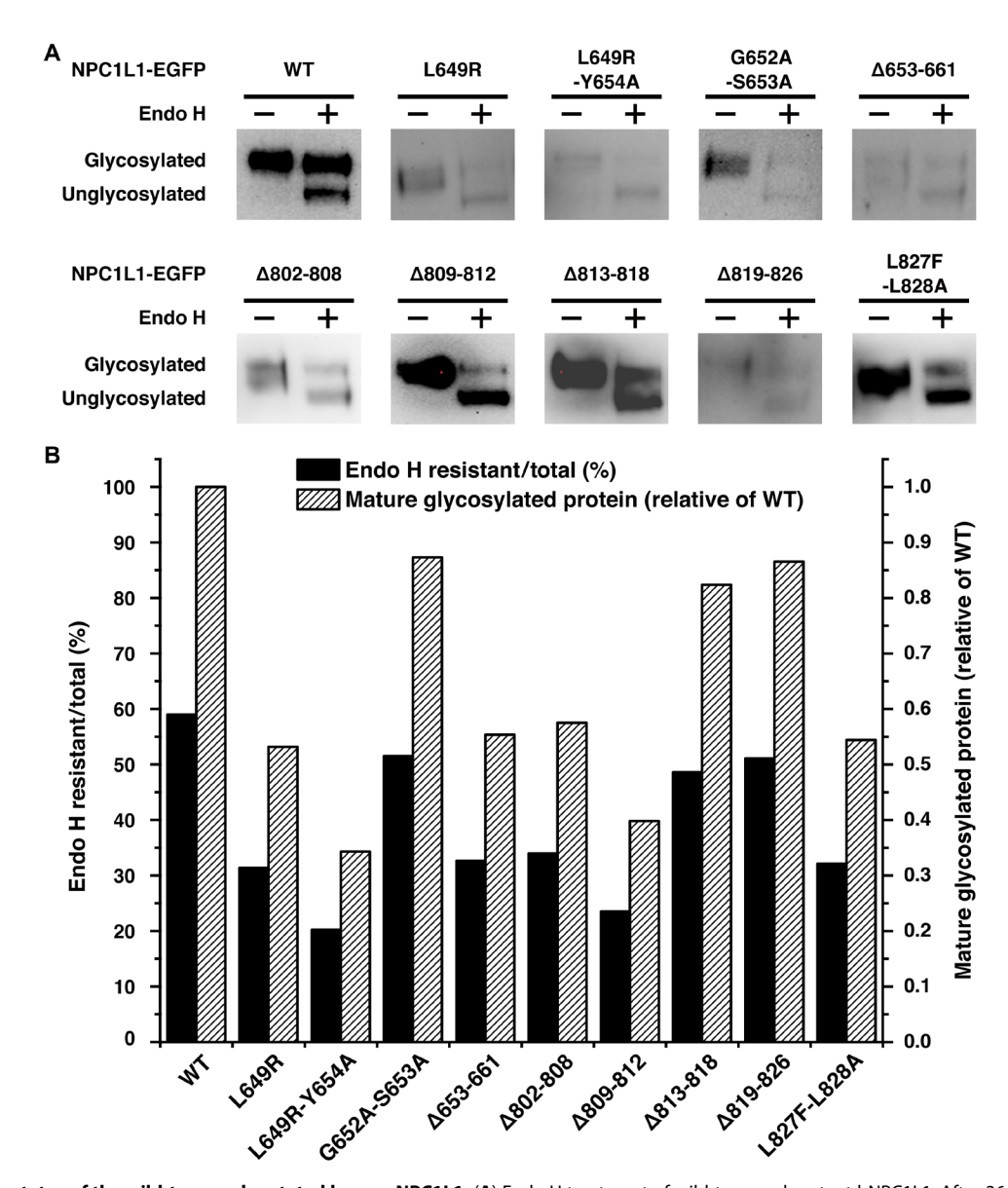


Fig. 6. Glycosylation status of the wild-type and mutated human NPC1L1. (A) Endo H treatment of wild-type and mutant hNPC1L1. After 36-hour transfection, the cell lysates were treated with Endo H as described in Materials and Methods. Then, the samples were analyzed by Western blot with anti–enhanced green fluorescent protein (EGFP) antibody. (B) Quantification of the Endo H–resistant hNPC1L1 shown in (A) by densitometry. After Endo H treatment, the ratio of Endo H resistant to total was calculated by dividing glycosylated plus unglycosylated protein by glycosylated protein. For calculation of the relative amount of the mature glycosylated protein, the ratio of Endo H resistant to total of the wild-type hNPC1L1 was normalized. Three independent experiments were performed, and one representative is presented in the figures.

 $\Delta653\text{-}661)$  showed only  $\sim\!15\%$  of the total protein migrating to PM, much lower than that of the wild-type NPC1L1. Moreover, the endocytosis of the PM-localized NPC1L1 after cholesterol replenishment was also attenuated for NPC1L1 mutants, compared with that of the wild-type NPC1L1. Similarly, the mutants related to CLR-6 only internalized less than  $\sim\!40\%$  of the PM-localized protein (Fig. 7, A and C), indicating that these mutations inhibited the protein endocytosis.

Together, our results indicated that the mutations in the residues participating in the interactions within the SSD cluster damaged the cellular cholesterol uptake mediated by NPC1L1, which is due to the impairment of the protein glycosylation, as well as the protein trafficking responding to cholesterol variations. Among these mutants, the mutations related to L649 and Y654 showed most severe defects in cholesterol uptake, protein glycosylation, and protein trafficking. As L649 and Y654 are two major residues for the CLR-6

binding, this phenomenon suggested that CLR-6 in the structural cluster is indispensable for the function of NPC1L1.

#### **DISCUSSION**

In this work, we resolved four structures of human NPC1L1: the FL-hNPC1L1 in the apo state, the NTD-deleted hNPC1L1 in the apo, the cholesterol-enriched state, and the EZE-bound state, respectively. One common feature of these structures is that a small molecule occupies the central cavity of each structure. However, the molecules are different among these structures: the DDM-like molecule in the FL-hNPC1L1-Apo,  $\Delta$ N-hNPC1L1-Apo, and  $\Delta$ N-hNPC1L1-CLR, whereas EZE in the  $\Delta$ N-hNPC1L1-CLR-EZE. When replenishing additional cholesterol molecules during the cell culture and the protein purification procedure, it was somewhat unexpected that the cavity in the NPC1L1 was still occupied by DDM but not

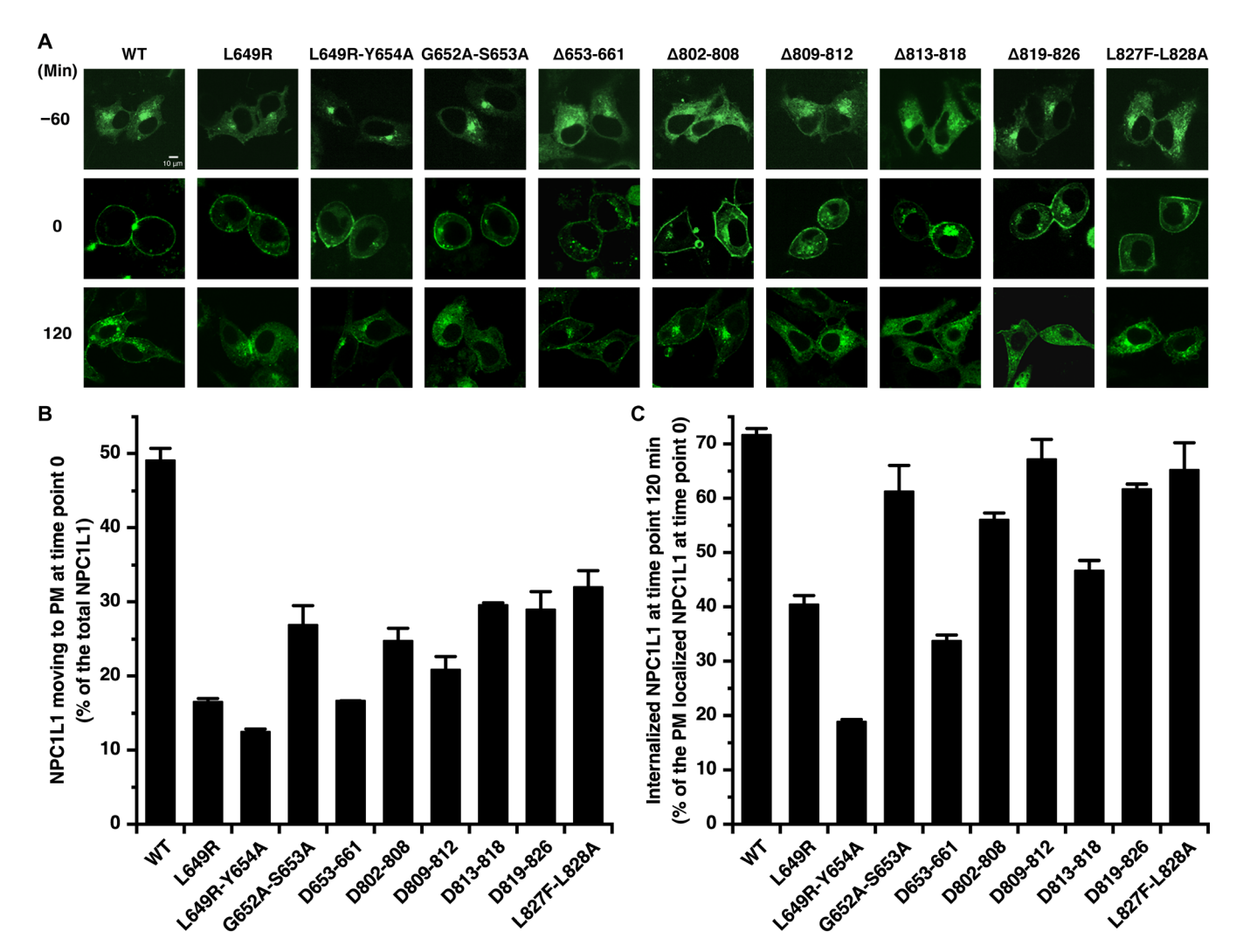


Fig. 7. Cholesterol-regulated trafficking of the wild-type and mutated human NPC1L1. (A) Cells transfected with wild-type and mutant hNPC1L1 were treated as shown in Fig. 5A. At various time points, cells were fixed and examined by confocal microscopy. Scale bar, 10 μm. (B) Fluorescence quantification of the hNPC1L1 protein moving to the PM upon cholesterol depletion, expressed as a percentage of the total hNPC1L1 protein. Error bars represent SDs. (C) Fluorescence quantification of the internalized hNPC1L1 protein after cholesterol replenishment, expressed as a percentage of the PM-localized hNPC1L1 protein at time point 0 min, as described in Materials and Methods. Error bars represent SDs.

cholesterol. This observation suggests that the cholesterol cannot compete with DDM binding. Nevertheless, addition of EZE resulted in the replacement of the DDM with the EZE in the cavity, indicating that the EZE has higher affinity with the protein and is very stable in the cavity, which is consistent with the potent inhibition effect of EZE.

Along with the different small molecules, NPC1L1 displays different conformations. The DDM-bound NPC1L1 is more stable than the EZE-bound NPC1L1, and, moreover, cholesterol further increases the stability of the protein (Fig. 4A). These phenomena are supported by the facts that the resolution of ΔN-hNPC1L1-CLR-EZE (3.37 Å) is lower than that of FL-hNPC1L1-Apo (3.03 Å), and the  $\Delta$ NhNPC1L1-CLR has the highest resolution (2.69 Å). Comparing these structures, the two lumenal domains are nearly identical, whereas the TMD is changed, and the most prominent difference occurs to SSD. In the case of the comparison between FL-hNPC1L1-Apo and ΔN-hNPC1L1-CLR, two differences are observed: One is two more cholesterol molecules (CLR-5 and CLR-6) binding to the SSD of ΔN-hNPC1L1-CLR, and the other one is that, at the cytoplasmic side of NPC1L1's SSD, a structural cluster formed by four elements one cholesterol (CLR-6), one PS-like lipid, and Loops 3-4 and 7-8 is clearly identified in the density map of  $\Delta$ N-hNPC1L1-CLR, whereas this cluster is unresolved in FL-hNPC1L1-Apo, or, strictly speaking, only some traces of the four elements could be observed in the density map of FL-hNPC1L1-Apo when we lowered the threshold of the map. Because FL-hNPC1L1-Apo is extracted from the normal cultured cells where a certain level of cholesterol exists, and  $\Delta N$ hNPC1L1-CLR is in a cholesterol-enriched state, i.e., in the higher level of cholesterol than FL-hNPC1L1-Apo, the structural differences between them suggest that SSD could respond to the abundant cholesterol by binding more cholesterol molecules, one of which, CLR-6, in turn, could trigger and directly participate in the formation of the structural cluster composed of CLR-6, PS-like lipid, and Loops 3-4 and 7-8. Along with the SSD structural cluster formation, the extensive interactions between the four elements make Loops 3-4 and 7-8 from the flexible state into the stable state. The point mutants and deletion mutants of these loops exhibited declined cholesterol uptake and impaired trafficking compared to the wild-type NPC1L1, suggesting that the conformational transition of Loops 3-4 and 7-8 is essential to the function of NPC1L1. It is worth noting that, similar to the CLR-6 in the NPC1L1, a binding site for cross-linkable cholesterol is identified within Loop 7-8 of the homolog NPC1 by using clickable, photoreactive sterol probes in combination with quantitative mass spectrometry (37), and Loop 7-8 is indispensable for NPC1-mediated cholesterol export (23). Thus, it seems that NPC1L1 and NPC1 may sense the environmental cholesterol level alteration via the cytoplasmic Loops 3-4 and 7-8 of the SSD domains.

Things are much different when it comes to the  $\Delta N$ -hNPC1L1-CLR-EZE. After EZE hijacks and enters deeply into the central cavity originally occupied by the DDM-like molecule in the apo or cholesterol-enriched state of NPC1L1, the SSD becomes deformed. First, the V-shaped SSD pocket becomes smaller, and its space cannot accommodate a cholesterol entirely as was observed in the  $\Delta N$ -hNPC1L1-CLR, which is consistent with the decreased interface area between CLR-1 and the pocket (from 327.1 Ų of  $\Delta N$ -hNPC1L1-CLR to 291.3 Ų of  $\Delta N$ -hNPC1L1-CLR-EZE). Second, the TMs in SSD and IH1 undergo concerted shifts, which destroy the interaction between the PS-like lipid and the protein and thus the formation of the structural cluster. As a result, the PS-like lipid, the CLR-6, and

Loops 3-4 and 7-8 are completely invisible in the density map of ΔN-hNPC1L1-CLR-EZE. Together, binding of EZE to the neck region and the bottom of the central cavity causes the deformation of the SSD, which further inhibits the function of NPC1L1. In addition, it has been reported that the formation of NPC1L1-flotillinpositive cholesterol-enriched membrane microdomains is essential for efficient cholesterol uptake, and EZE disrupts the association between NPC1L1 and flotillins, which blocks the formation of the cholesterol-enriched microdomains (29). On the basis of these points and our finding that EZE destroys the stability of Loops 3-4 and 7-8, it is therefore very plausible that Loops 3-4 and 7-8 are the binding sites for flotillins. Abundant cholesterol could stabilize Loops 3-4 and 7-8 to facilitate the binding with flotillins, while EZE impairs the loops' stability to break the association with flotillins and the formation of the NPC1L1-flotillin-cholesterol membrane microdomains. Actually, similar mechanism is also found in another SSD-containing protein, SCAP. The Met-Glu-Leu-Ala-Asp-Leu sequence in Loop 6 in SCAP SSD is used to bind coat protein complex II, triggering ER-to-Golgi transport of SCAP (38). Because Loop 7-8 in NPC1L1 SSD is exactly the counterpart of Loop 6 in SCAP SSD, it is possible that a sequence in Loop 7-8 of NPC1L1 SSD could be used to bind a regulatory protein, such as flotillin, to mediate the recruitment of NPC1L1 into the cholesterol-enriched membrane microdomains. However, other mechanisms may also exist, such as the formation of the SSD structural cluster in response to high cholesterol level might move the protein into the cholesterol-enriched membrane microdomains by means of lateral segregation. Therefore, these mechanisms need to be further investigated. It should be mentioned that, recently, Huang et al. (16) published the structure of EZE-PS-bound rat NPC1L1. Because EZE-PS has two larger side chains than EZE, it was stuck at the entrance of the central cavity (16). They suggested that the stuck EZE-PS could block the cholesterol transport by occluding the tunnel for cholesterol (16). Because EZE has multiple metabolites with distinct chemical structures after oral administration, they might have different inhibition mechanisms of NPC1L1 (39, 40).

One remaining question is what the molecule is in the central cavity of the neck region under physiological conditions. In our work, we only observed DDM in this site in the structures of FL-hNPC1L1-Apo, ΔN-hNPC1L1-Apo, and ΔN-hNPC1L1-CLR. One possible reason is that the protein was purified using a large amount of DDM, and DDM might be able to compete with the endogenous molecule, such as cholesterol, binding to the central cavity. Actually, some densities were also seen in the structures of FL-rNPC1L1-Apo (16) and NPC1 (26) and were modeled as cholesterol by the researchers. Therefore, although our structures cannot determine the molecule in the central cavity, we cannot rule out that it might be a cholesterol molecule. Nevertheless, our work finds a novel structural feature of NPC1L1, the cluster at the cytoplasmic side of SSD. The formation of this cluster is sensitive to the cholesterol concentration, and EZE can disrupt this cluster, which provides structural insights into the mechanisms of NPC1L1 function and EZE inhibition.

### **MATERIALS AND METHODS**

#### **Cell culture**

The Escherichia coli cells' DH5α were cultured in LB (Sigma-Aldrich) and TB (Sigma-Aldrich) medium at 37°C. HEK293F suspension cells were cultured in FreeStyle 293 medium (Thermo Fisher Scientific)

supplemented with penicillin-streptomycin (100 U/ml; Gibco) at 37°C with 5% CO<sub>2</sub>. McArdle RH7777 rat hepatoma cells (ATCC-CRL1601) were grown in monolayer at 37°C with 5% CO<sub>2</sub>. The cells were maintained in medium A [Dulbecco's minimum essential medium from Gibco containing penicillin-streptomycin (100 U/ml)] supplemented with 10% fetal bovine serum (from Gibco). Cholesteroldepleting medium was medium A supplemented with 5% lipoprotiendeficient serum (LPDS; from Sigma-Aldrich), 50 µM mevalonate (Sigma-Aldrich), 1 μM lovastatin (Selleckchem), and 1% methyl-βcyclodextrin (CDX; from Sigma-Aldrich). Cholesterol-replenishing medium was medium A supplemented with 5% LPDS, 50 µM mevalonate, 1 µM lovastatin, and cholesterol-CDX (15 µg/ml). The cholesterol-CDX inclusion complexes were prepared as described previously (41). Plasmid transfection was carried out using Lipofectamine 2000 reagent (Thermo Fisher Scientific) according to the manufacturer's instruction.

#### Protein expression and purification

The complementary DNA of FL-hNPC1L1 was cloned into a vector pCMV-3×FLAG containing a C-terminal FLAG tag. When the density of HEK293F cells reached  $2.0\times10^6$  cells/ml, the cells were transiently transfected with the expression plasmids using polyethylenimines (PEIs) (Polysciences). Approximately 2 mg of plasmids and 3 mg of PEIs, each in 25 ml of fresh medium, were premixed for 30 min, and then the 50 ml of mixture was added to 800 ml of cell cultures. Transfected cells were cultured for 48 hours before harvesting.

For purification of FL-hNPC1L1-Apo and ΔN-hNPC1L1-Apo, the collected cells were solubilized in the lysis buffer containing 20 mM Hepes (pH 7.4), 150 mM NaCl, 1% DDM (Anatrace), and protease inhibitor cocktails (Roche) at 4°C for 1 hour. After centrifugation at 25,000g for 1 hour, the supernatant was collected and incubated with FLAG affinity resin (Sigma-Aldrich) at 4°C for 1 hour. The resin was rinsed with the wash buffer 1 of 20 mM Hepes (pH 7.4), 150 mM NaCl, and 0.05% DDM and then with wash buffer 2 of 20 mM Hepes (pH 7.4), 150 mM NaCl, and 0.1% Digitonin (Sigma-Aldrich). Then, the protein was eluted with elution buffer of 20 mM Hepes (pH 7.4), 150 mM NaCl, 0.1% Digitonin, and FLAG peptide (0.1 mg/ml; Sigma-Aldrich). The eluted protein was applied to size exclusion chromatography (SEC; superpose 200 increase, GE Healthcare) with the buffer of 20 mM Hepes (pH 7.4), 150 mM NaCl, and 0.1% digitonin. Last, the protein was concentrated to 6 to 10 mg/ml for the cryo-EM sample preparation. For ΔN-hNPC1L1-CLR-EZE, the protein of ΔN-hNPC1L1-CLR was incubated with EZE at a molar ratio of 1:10 at room temperature for 30 min before making the cryo-EM sample.

For ΔN-NPC1L1-CLR, the HEK293F cells were transiently transfected with the expression plasmids for 48 hours, and 0.005% cholesterol (Sigma-Aldrich) in methanol was replenished to the cell culture. The cells were collected and solubilized in lysis buffer containing 20 mM Hepes (pH 7.4), 150 mM NaCl, 1% DDM, 0.005% cholesterol, and protease inhibitor cocktails at 4°C for 1 hour. After centrifugation at 25,000g for 1 hour, the supernatant was collected and incubated with FLAG affinity resin at 4°C for 1 hour. The resin was rinsed with the washed buffer 1 supplemented with 0.005% cholesterol and then with wash buffer 2 supplemented with 0.005% cholesterol. The protein was eluted with the elution buffer of 20 mM Hepes (pH 7.4), 150 mM NaCl, 0.1% Digitonin, FLAG peptide (0.1 mg/ml), and 0.005% cholesterol. The eluted protein was applied to SEC (superpose 200 increase, GE Healthcare) with the buffer of 20 mM Hepes (pH 7.4), 150 mM NaCl, 0.1% Digitonin, and 0.005%

cholesterol. Last, the protein was concentrated to 6 to 10 mg/ml and incubated with 0.005% cholesterol for 30 min at 4°C before preparing the cryo-EM samples. Cholesterol was originally resolved in the methanol at 1.2%.

#### **Cryo-EM sample preparation and processing**

Aliquots of prepared proteins were applied to freshly glow-discharged holey carbon grids (Quantifoil Au R1.2/1.3 400 mesh). Then, the grids were blotted for 4 s and plunged into liquid ethane cooled with liquid nitrogen with Vitrobot Mark IV (Thermo Fisher Scientific). The cryo-EM data were collected using a Titan Krios Microscope (Thermo Fisher Scientific) operated at 300 kV and equipped with a K2 or K3 Summit direct electron detector (Gatan) and a GIF Quantum energy filter (Gatan). The cryo-EM images were automatically collected using AutoEMation (42) with a slit width of 20 eV on the energy filter and a preset defocus range of -1.8 to -1.3 µm in superresolution mode at a nominal magnification of  $\times 105,000$  or  $\times 130,000$ . Each stack was exposed for 8 s with an exposure time of 0.25 s per frame and recorded as a movie of 32 frames, resulting in the total dose rate of approximately 50 electrons/Å<sup>2</sup> for each movie stack. The stacks were motion-corrected with MotionCor2 (43) and binned twofold, resulting in a pixel size of 0.8433, 1.091, or 1.061 Å per pixel (details could be found in table S1). The average of each movie stack was calculated and summed, resulting in nondose-weighted average for contrast transfer function (CTF) estimation with Gctf (44) and dose-weighted average for reconstruction with RELION-2.0/RELION-3.0 (45-47).

The data processing procedures of three samples, FL-hNPC1L1-Apo, ΔN-hNPC1L1-Apo, and ΔN-hNPC1L1-CLR, are almost the same. Taking the FL-NPC1L1-Apo as an example, we collected a total of 4431 movies, and 1,918,878 particles were autopicked in RELION-3.0. After 2D classification, 1,096,746 particles were selected and subjected to a global angular searching 3D classification with only one class. The initial model was generated by EMAN2 (48) using the common-line method by the 2D classification images. For each of the last several iterations of the global angular searching 3D classification, a local angular searching 3D classification was performed with four classes. The good classes of each local angular searching 3D classification were merged, and the duplicated particles were removed. The resulting total 247,913 particles were subjected to several rounds of multireference 3D classification. Last, a total of 220,927 particles were selected and subjected to a 3D autorefinement with an overall mask, resulting in a 3.03 Å resolution map after postprocessing. For ΔN-hNPC1L1-Apo and ΔN-hNPC1L1-CLR, totals of 2,164,284 and 1,915,958 particles were autopicked from 2,958 and 4,418 micrographs, respectively. After 2D classification, 1,443,663 and 1,617,287 particles were selected and subjected to the global angular searching 3D classification. After this step, 972,166 and 1,133,272 particles were applied to the multireference classification. The final resolution was 3.14 Å for  $\Delta$ N-hNPC1L1-Apo with a final particle number of 200,253 and 2.69 Å for ΔN-hNPC1L1-CLR with a final particle number of 317,081.

For ΔN-ĥNPC1L1-CLR-EZE, we collected a total of 2852 movies, and 655,821 particles were autopicked in RELION-3.0. The particles were imported into cryoSPARC software (49). After two rounds of 2D classification, 308,304 particles were selected and subjected to ab initio reconstruction and heterogeneous refinement sequentially in cryoSPARC. Last, 168,403 particles were selected and imported into RELION. The local search refinement by RELION-3.1 was applied to these particles, and the final resolution was 3.37 Å.

#### Model building and refinement

For building the model of the human NPC1L1, the crystal structure of NPC1 [Protein Data Bank (PDB) code 5 U74] (50), which shares 42% identity with NPC1L1, was docked into the density map using Chimera (51). Then, the sequence of NPC1 was replaced with corresponding residues in the NPC1L1 in Coot (52), and the sequence assignments were guided by well-resolved bulky residues such as phenylalanine, tyrosine, tryptophan, and arginine. The structure was manually adjusted on the basis of the density map in Coot. The NTD and C-terminal sequences of NPC1L1 were not modeled as the corresponding densities were not visible on the map. Ten sugar moieties were built according to the map density. A DDM molecule was assigned to the density lobe in the central cavity for structures of FL-hNPC1L1-Apo and ΔN-hNPC1L1-CLR. Four and six cholesterol molecules were assigned into the densities surrounding the TMD of structures of FL-hNPC1L1-Apo and ΔN-hNPC1L1-CLR-EZE, and ΔN-hNPC1L1-CLR, respectively. A PS lipid was modeled according to the map density. The EZE was built using "phenix.elbow" in PHENIX (53) and modeled on the basis of the map density.

All the models were refined against the corresponding density maps with "phenix.real\_space\_refine" in PHENIX, with secondary structural and geometric restraints to prevent structure overfitting. The final atomic models were cross-validated according to previously described procedures (54, 55). Briefly, atoms in the model were randomly shifted by up to 0.5 Å and then refined against one of the two independent half maps generated during the final 3D reconstruction. Then, the refined model was tested against the other map. The data collection, model refinement, and validation statistics are presented in table S1. The statistics of the geometries of the models were generated using MolProbity (56). All the figures were prepared in PyMOL (https://pymol.org/2/) or Chimera (www.cgl.ucsf.edu/chimera/) (51). The sequence alignments were performed by Clustal W (57) and created by ESPript (58).

# Fluorescence quenching analysis of the EZE-binding affinity of NPC1L1

Quantitative analysis of the EZE-binding abilities of wild-type and mutated NPC1L1 proteins was monitored by the quenching of the intrinsic tryptophan fluorescence spectra (59). To generate the data shown in Fig. 3E, a dilution series of EZE molecule in the methanol was incubated with wild-type and mutated NPC1L1 proteins (0.15 mg/ml) in the binding buffer [20 mM Hepes (pH 7.4), 150 mM NaCl, and 0.05% DDM] at 25°C for 15 min before measuring fluorescence intensity using excitation/emission wavelengths of 344/295 nm on a microplate reader (EnSpire). Dissociation constants  $(K_{\rm d} \text{ values})$  were evaluated by fitting the data to the equation,  $\log \left[\frac{F_0 - F}{F}\right] = \log \left(\frac{1}{K_{\rm d}}\right) + n \log [Q]$  (59), where  $F_0$  and F are the fluorescence intensities of the protein without EZE and in the presence of EZE, respectively; *n* is the number of the binding sites; and [Q] is the concentration of EZE, using Origin 8 software (OriginLab Corporation). Error bars show the SDs. The data for each protein are calculated from three independent experiments, one of which is shown in the figures.

## Filipin staining

A fresh solution of filipin (5 mg/ml; PeproTech) was prepared in dimethyl sulfoxide. Cells were fixed with 4% paraformaldehyde, washed three times with PBS, and then stained with filipin (50  $\mu$ g/ml) in the dark for 30 min at room temperate. Filipin signals of stained

cells were analyzed with confocal microscope FV3000 (Olympus) using an excitatory wavelength of 405 nm. Red color was assigned to show the filipin signal. In each experiment, images were acquired at identical laser parameters.

#### In vitro glycosylation assay

Thirty-six hours after transfection, cells were harvested and lysed in the buffer of 20 mM Hepes (pH 7.4), 150 mM NaCl, 1% DDM, 1 mM phenylmethylsulfonyl fluoride, and protease inhibitor cocktail. The cell lysate was centrifuged at 25,000g for 40 min at 4°C, and then the supernatant was treated with or without Endo H by following the instructions. Immunoblot analysis was carried out using anti–green fluorescent protein (GFP) antibody. Quantification of the Endo H–resistant NPC1L1 by densitometry was performed as previously described (36). For calculation of the relative amount of the mature glycosylated protein, the ratio of Endo H resistant to total of the wild-type NPC1L1 was arbitrarily defined as 1, against which the ratio of Endo H resistant to total of mutant NPC1L1 was normalized. Three independent experiments were performed, and one representative is presented in the figure.

#### Fluorescence quantification

The procedure for fluorescence quantification was referred to previous reports (31, 36). The ImageJ software was used for data analysis (https://imagej.net/Fiji).

For quantification of the cellular cholesterol uptake, one boundary outlining the whole cell was drawn manually (fig. S8). After subtraction of the background, the fluorescence intensities of filipin signals were regarded as the total cellular cholesterol, and enhanced GFP signals as the expressed NPC1L1 protein. The increase of the cholesterol uptake mediated by the overexpression of NPC1L1 was calculated as follows: fold of increased cholesterol, obtained from total cellular cholesterol of transfected cells divided by that of nontransfected cells, minus 1. Values were further normalized to the expressed NPC1L1 protein. Approximately 50 cells were calculated for each mutant. Three independent experiments were performed, and one representative is presented in the figure.

For quantification of the NPC1L1 protein trafficking, two boundaries, one beneath the PM and the other one outlining the whole cell, were drawn manually (fig. S8). After subtraction of the background, the fluorescence intensities in each boundary were measured and regarded as whole-cell and intracellular fluorescence intensity, respectively. PM intensity was obtained using the whole-cell intensity minus the intracellular intensity. The intensity of each cell was defined as 1, against which the PM intensity was normalized. The NPC1L1 protein moving to the PM upon cholesterol depletion was calculated by subtracting PM intensity at time point -60 min from that at time point 0 min. The internalized NPC1L1 protein after cholesterol replenishment was calculated as follows: the PM intensity at time point 120 min minus that at time point 0 min, and the value was further normalized to the PM intensity at time point 120 min. Approximately 50 cells were calculated for each mutant. Three independent experiments were performed, and one representative is presented in the figure.

#### **SUPPLEMENTARY MATERIALS**

Supplementary material for this article is available at http://advances.sciencemag.org/cgi/content/full/7/29/eabg3188/DC1

View/request a protocol for this paper from Bio-protocol.

#### **REFERENCES AND NOTES**

- 1. S.-W. Park, Intestinal and hepatic Niemann-pick C1-like 1. Diabetes Metab. J. 37, 240–248 (2013).
- R. A. Kreisberg, A. Oberman, Clinical review 141: Lipids and atherosclerosis: Lessons learned from randomized controlled trials of lipid lowering and other relevant studies. *J. Clin. Endocrinol. Metab.* 87, 423–437 (2002).
- D. Lloyd-Jones, R. J. Adams, T. M. Brown, M. Carnethon, S. Dai, G. De Simone,
  T. Bruce Ferguson, E. Ford, K. Furie, C. Gillespie, A. Go, K. Greenlund, N. Haase, S. Hailpern,
  P. Michael Ho, V. Howard, B. Kissela, S. Kittner, D. Lackland, L. Lisabeth, A. Marelli,
  M. M. McDermott, J. Meigs, D. Mozaffarian, M. Mussolino, G. Nichol, V. L. Roger,
  W. Rosamond, R. Sacco, P. Sorlie, R. Stafford, T. Thom, S. Wasserthiel-Smoller, N. D. Wong,
  J. Wylie-Rosett; American Heart Association Statistics Committee, S. S. Subcommittee,
  Executive summary: Heart disease and stroke statistics—2010 update: A report
  from the American Heart Association. Circulation 121, 948–954 (2010).
- J. Luo, H. Yang, B.-L. Song, Mechanisms and regulation of cholesterol homeostasis. Nat. Rev. Mol. Cell Biol. 21, 225–245 (2020).
- J. A. Tobert, Lovastatin and beyond: The history of the HMG-CoA reductase inhibitors. Nat. Rev. Drug Discov. 2, 517–526 (2003).
- M. H. Davidson, T. McGarry, R. Bettis, L. Melani, L. J. Lipka, A. P. LeBeaut, R. Suresh, S. Sun, E. P. Veltri, Ezetimibe coadministered with simvastatin in patients with primary hypercholesterolemia. *J. Am. Coll. Cardiol.* 40, 2125–2134 (2002).
- C. Gagné, H. E. Bays, S. R. Weiss, P. Mata, K. Quinto, M. Melino, M. Cho, T. A. Musliner, B. Gumbiner; Ezetimibe Study Group, Efficacy and safety of ezetimibe added to ongoing statin therapy for treatment of patients with primary hypercholesterolemia. *Am.* J. Cardiol. 90, 1084–1091 (2002).
- S. B. Rosenblum, T. Huynh, A. Afonso, H. R. Davis Jr., N. Yumibe, J. W. Clader, D. A. Burnett, Discovery of 1-(4-fluorophenyl)-(3R)-[3-(4-fluorophenyl)-(3S)-hydroxypropyl]-(4S)-(4-hydroxyphenyl)-2-azetidinone (SCH 58235): A designed, potent, orally active inhibitor of cholesterol absorption. J. Med. Chem. 41, 973–980 (1998).
- H. R. Davis Jr., K. K. Pula, K. B. Alton, R. E. Burrier, R. W. Watkins, The synergistic hypocholesterolemic activity of the potent cholesterol absorption inhibitor, ezetimibe, in combination with 3-hydroxy-3-methylglutaryl coenzyme a reductase inhibitors in dogs. *Metab. Clin. Exp.* 50, 1234–1241 (2001).
- H. R. Davis Jr., L.-J. Zhu, L. M. Hoos, G. Tetzloff, M. Maguire, J. Liu, X. Yao, S. P. N. Iyer, M.-H. Lam, E. G. Lund, P. A. Detmers, M. P. Graziano, S. W. Altmann, Niemann-Pick C1 Like 1 (NPC1L1) is the intestinal phytosterol and cholesterol transporter and a key modulator of whole-body cholesterol homeostasis. J. Biol. Chem. 279, 33586–33592 (2004).
- H. R. Davis, S. W. Altmann, Niemann-Pick C1 Like 1 (NPC1L1) an intestinal sterol transporter. *Biochim. Biophys. Acta* 1791, 679–683 (2009).
- M. Garcia-Calvo, J. Lisnock, H. G. Bull, B. E. Hawes, D. A. Burnett, M. P. Braun, J. H. Crona, H. R. Davis, D. C. Dean, P. A. Detmers, M. P. Graziano, M. Hughes, D. E. MacIntyre, A. Ogawa, K. A. O'Neill, S. P. N. Iyer, D. E. Shevell, M. M. Smith, Y. S. Tang, A. M. Makarewicz, F. Ujjainwalla, S. W. Altmann, K. T. Chapman, N. A. Thornberry, The target of ezetimibe is Niemann-Pick C1-Like 1 (NPC1L1). Proc. Natl. Acad. Sci. U.S.A. 102, 8132–8137 (2005).
- L. Jia, J. L. Betters, L. Yu, Niemann-pick C1-like 1 (NPC1L1) protein in intestinal and hepatic cholesterol transport. *Annu. Rev. Physiol.* 73, 239–259 (2011).
- J.-H. Zhang, L. Ge, W. Qi, L. Zhang, H.-H. Miao, B.-L. Li, M. Yang, B.-L. Song, The N-terminal domain of NPC1L1 protein binds cholesterol and plays essential roles in cholesterol uptake. J. Biol. Chem. 286, 25088–25097 (2011).
- A. B. Weinglass, M. Kohler, U. Schulte, J. Liu, E. O. Nketiah, A. Thomas, W. Schmalhofer, B. Williams, W. Bildl, D. R. McMasters, K. Dai, L. Beers, M. E. McCann, G. J. Kaczorowski, M. L. Garcia, Extracellular loop C of NPC1L1 is important for binding to ezetimibe. *Proc. Natl. Acad. Sci. U.S.A.* 105, 11140–11145 (2008).
- C.-S. Huang, X. Yu, P. Fordstrom, K. Choi, B. C. Chung, S.-H. Roh, W. Chiu, M. Zhou, X. Min, Z. Wang, X. Yu, P. Fordstrom, K. Choi, B. C. Chung, S.-H. Roh, W. Chiu, M. Zhou, X. Min, Z. Wang, Cryo-EM structures of NPC1L1 reveal mechanisms of cholesterol transport and ezetimibe inhibition. Sci. Adv. 6, eabb1989 (2020).
- P. E. Kuwabara, M. Labouesse, The sterol-sensing domain: multiple families, a unique role? Trends Genet. 18, 193–201 (2002).
- X. Gong, H. Qian, X. Zhou, J. Wu, T. Wan, P. Cao, W. Huang, X. Zhao, X. Wang, P. Wang, Y. Shi, G. F. Gao, Q. Zhou, N. Yan, Structural insights into the Niemann-Pick C1 (NPC1)-mediated cholesterol transfer and ebola infection. *Cell* 165, 1467–1478 (2016).
- Y. A. Moon, The SCAP/SREBP pathway: A mediator of hepatic steatosis. Endocrinol. Metab. (Seoul) 32, 6–10 (2017).
- E. S. Istvan, M. Palnitkar, S. K. Buchanan, J. Deisenhofer, Crystal structure of the catalytic portion of human HMG-CoA reductase: Insights into regulation of activity and catalysis. EMBO J. 19, 819–830 (2000).
- Y. Zhang, D. P. Bulkley, Y. Xin, K. J. Roberts, D. E. Asarnow, A. Sharma, B. R. Myers, W. Cho, Y. Cheng, P. A. Beachy, Structural basis for cholesterol transport-like activity of the hedgehog receptor patched. *Cell* 175, 1352–1364.e14 (2018).
- 22. F. Cannac, C. Qi, J. Falschlunger, G. Hausmann, K. Basler, V. M. Korkhov, Cryo-EM structure of the Hedgehog release protein Dispatched. *Sci. Adv.* **6**, eaay7928 (2020).

- P. Saha, J. L. Shumate, J. G. Caldwell, N. Elghobashi-Meinhardt, A. Lu, L. Zhang,
   N. E. Olsson, J. E. Elias, S. R. Pfeffer, Inter-domain dynamics drive cholesterol transport by
   NPC1 and NPC1L1 proteins. *eLife* 9, e57089 (2020).
- P.-S. Li, Z.-Y. Fu, Y.-Y. Zhang, J.-H. Zhang, C.-Q. Xu, Y.-T. Ma, B.-L. Li, B.-L. Song, The clathrin adaptor Numb regulates intestinal cholesterol absorption through dynamic interaction with NPC1L1. Nat. Med. 20. 80–86 (2014).
- M. B. L. Winkler, R. T. Kidmose, M. Szomek, K. Thaysen, S. Rawson, S. P. Muench,
   D. Wüstner, B. P. Pedersen, Structural insight into eukaryotic sterol transport through Niemann-Pick type C proteins. Cell 179, 485–497.e18 (2019).
- H. Qian, X. Wu, X. Du, X. Yao, X. Zhao, J. Lee, H. Yang, N. Yan, Structural basis of low-pHdependent lysosomal cholesterol egress by NPC1 and NPC2. Cell 182, 98–111.e18 (2020).
- L. Yu, S. Bharadwaj, J. M. Brown, Y. Ma, W. du, M. A. Davis, P. Michaely, P. Liu, M. C. Willingham, L. L. Rudel, Cholesterol-regulated translocation of NPC1L1 to the cell surface facilitates free cholesterol uptake. *J. Biol. Chem.* 281, 6616–6624 (2006).
- M. A. Valasek, J. Weng, P. W. Shaul, R. G. W. Anderson, J. J. Repa, Caveolin-1 is not required for murine intestinal cholesterol transport. *J. Biol. Chem.* 280, 28103–28109 (2005).
- L. Ge, W. Qi, L.-J. Wang, H.-H. Miao, Y.-X. Qu, B.-L. Li, B.-L. Song, Flotillins play an essential role in Niemann-Pick C1-like 1-mediated cholesterol uptake. *Proc. Natl. Acad. Sci. U.S.A.* 108, 551–556 (2011).
- Y.-Y. Zhang, Z.-Y. Fu, J. Wei, W. Qi, G. Baituola, J. Luo, Y.-J. Meng, S.-Y. Guo, H. Yin, S.-Y. Jiang, Y.-F. Li, H.-H. Miao, Y. Liu, Y. Wang, B.-L. Li, Y.-T. Ma, B.-L. Song, A LIMA1 variant promotes low plasma LDL cholesterol and decreases intestinal cholesterol absorption. Science 360, 1087–1092 (2018).
- L. Ge, J. Wang, W. Qi, H.-H. Miao, J. Cao, Y.-X. Qu, B.-L. Li, B.-L. Song, The cholesterol absorption inhibitor ezetimibe acts by blocking the sterol-induced internalization of NPC1L1. *Cell Metab.* 7, 508–519 (2008).
- X. Gong, H. Qian, P. Cao, X. Zhao, Q. Zhou, J. Lei, N. Yan, Structural basis for the recognition of Sonic Hedgehog by human Patched 1. Science 361, eaas8935 (2018).
- F. Lu, Q. Liang, L. Abi-Mosleh, A. Das, J. K. De Brabander, J. L. Goldstein, M. S. Brown, Identification of NPC1 as the target of U18666A, an inhibitor of lysosomal cholesterol export and Ebola infection. *eLife* 4, e12177 (2015).
- J. Fantini, F. J. Barrantes, How cholesterol interacts with membrane proteins:
   An exploration of cholesterol-binding sites including CRAC, CARC, and tilted domains.

   Front. Physiol. 4, 31 (2013).
- A. Pirillo, A. L. Catapano, G. D. Norata, Niemann-Pick C1-Like 1 (NPC1L1) inhibition and cardiovascular diseases. Curr. Med. Chem. 23, 983–999 (2016).
- L.-J. Wang, J. Wang, N. Li, L. Ge, B.-L. Li, B.-L. Song, Molecular characterization of the NPC1L1 variants identified from cholesterol low absorbers. J. Biol. Chem. 286, 7397–7408 (2011).
- J. J. Hulce, A. B. Cognetta, M. J. Niphakis, S. E. Tully, B. F. Cravatt, Proteome-wide mapping of cholesterol-interacting proteins in mammalian cells. *Nat. Methods* 10, 259–264 (2013).
- M. S. Brown, A. Radhakrishnan, J. L. Goldstein, Retrospective on cholesterol homeostasis: The central role of Scap. Annu. Rev. Biochem. 87, 783–807 (2018).
- J. Wang, B.-B. Chu, L. Ge, B.-L. Li, Y. Yan, B.-L. Song, Membrane topology of human NPC1L1, a key protein in enterohepatic cholesterol absorption. *J. Lipid Res.* 50, 1653–1662 (2009).
- J. W. Clader, The discovery of ezetimibe: A view from outside the receptor. J. Med. Chem.
   47, 1–9 (2004).
- A. J. Brown, L. Sun, J. D. Feramisco, M. S. Brown, J. L. Goldstein, Cholesterol addition to ER membranes alters conformation of SCAP, the SREBP escort protein that regulates cholesterol metabolism. *Mol. Cell* 10, 237–245 (2002).
- 42. J. Lei, J. Frank, Automated acquisition of cryo-electron micrographs for single particle reconstruction on an FEI Tecnai electron microscope. *J. Struct. Biol.* **150**, 69–80 (2005).
- S. Q. Zheng, E. Palovcak, J.-P. Armache, K. A. Verba, Y. Cheng, D. A. Agard, MotionCor2: Anisotropic correction of beam-induced motion for improved cryo-electron microscopy. *Nat. Methods* 14, 331–332 (2017).
- K. Zhang, Gctf: Real-time CTF determination and correction. J. Struct. Biol. 193, 1–12 (2016).
- S. H. W. Scheres, RELION: Implementation of a Bayesian approach to cryo-EM structure determination. J. Struct. Biol. 180, 519–530 (2012).
- D. Kimanius, B. O. Forsberg, S. H. W. Scheres, E. Lindahl, Accelerated cryo-EM structure determination with parallelisation using GPUs in RELION-2. eLife 5, e18722 (2016).
- J. Zivanov, T. Nakane, B. O. Forsberg, D. Kimanius, W. J. H. Hagen, E. Lindahl, S. H. W. Scheres, New tools for automated high-resolution cryo-EM structure determination in RELION-3. *eLife* 7, e42166 (2018).
- G. Tang, L. Peng, P. R. Baldwin, D. S. Mann, W. Jiang, I. Rees, S. J. Ludtke, EMAN2: An extensible image processing suite for electron microscopy. *J. Struct. Biol.* 157, 38–46 (2007)
- A. Punjani, J. L. Rubinstein, D. J. Fleet, M. A. Brubaker, cryoSPARC: Algorithms for rapid unsupervised cryo-EM structure determination. *Nat. Methods* 14, 290–296 (2017).

#### SCIENCE ADVANCES | RESEARCH ARTICLE

- X. Li, F. Lu, M. N. Trinh, P. Schmiege, J. Seemann, J. Wang, G. Blobel, 3.3 Å structure of Niemann-Pick C1 protein reveals insights into the function of the C-terminal luminal domain in cholesterol transport. *Proc. Natl. Acad. Sci. U.S.A.* 114, 9116–9121 (2017).
- E. F. Pettersen, T. D. Goddard, C. C. Huang, G. S. Couch, D. M. Greenblatt, E. C. Meng, T. E. Ferrin, UCSF Chimera—A visualization system for exploratory research and analysis. J. Comput. Chem. 25, 1605–1612 (2004).
- P. Emsley, B. Lohkamp, W. G. Scott, K. Cowtan, Features and development of Coot. Acta Crystallogr. D Biol. Crystallogr. 66, 486–501 (2010).
- P. D. Adams, P. V. Afonine, G. Bunkóczi, V. B. Chen, I. W. Davis, N. Echols, J. J. Headd, L. W. Hung, G. J. Kapral, R. W. Grosse-Kunstleve, A. J. McCoy, N. W. Moriarty, R. Oeffner, R. J. Read, D. C. Richardson, J. S. Richardson, T. C. Terwilliger, P. H. Zwart, PHENIX: A comprehensive Python-based system for macromolecular structure solution. *Acta Crystallogr. D Biol. Crystallogr.* 66, 213–221 (2010).
- P. V. Afonine, B. P. Klaholz, N. W. Moriarty, B. K. Poon, O. V. Sobolev, T. C. Terwilliger,
   P. D. Adams, A. Urzhumtsev, New tools for the analysis and validation of cryo-EM maps and atomic models. *Acta Crystallogr. D Struct. Biol.* 74, 814–840 (2018).
- A. Amunts, A. Brown, X.-C. Bai, J. L. Llácer, T. Hussain, P. Emsley, F. Long, G. Murshudov,
   H. W. Scheres, V. Ramakrishnan, Structure of the yeast mitochondrial large ribosomal subunit. Science 343, 1485–1489 (2014).
- C. J. Williams, J. J. Headd, N. W. Moriarty, M. G. Prisant, L. L. Videau, L. N. Deis, V. Verma,
   D. A. Keedy, B. J. Hintze, V. B. Chen, S. Jain, S. M. Lewis, W. B. Arendall III, J. Snoeyink,
   P. D. Adams, S. C. Lovell, J. S. Richardson, D. C. Richardson, MolProbity: More and better reference data for improved all-atom structure validation. *Protein Sci.* 27, 293–315 (2018).
- M. A. Larkin, G. Blackshields, N. P. Brown, R. Chenna, P. A. McGettigan, H. McWilliam, F. Valentin, I. M. Wallace, A. Wilm, R. Lopez, J. D. Thompson, T. J. Gibson, D. G. Higgins, Clustal W and Clustal X version 2.0. *Bioinformatics* 23, 2947–2948 (2007).
- X. Robert, P. Gouet, Deciphering key features in protein structures with the new ENDscript server. *Nucleic Acids Res.* 42, W320–W324 (2014).
- A. A. Rhodes, B. L. Swartz, E. R. Hosler, D. L. Snyder, K. M. Benitez, B. S. Chohan, S. Basu, Static quenching of tryptophan fluorescence in proteins by a dioxomolybdenum(VI) thiolate complex. J. Photochem. Photobiol. A Chem. 293, 81–87 (2014).

Acknowledgments: We are grateful to B.-L. Song (Wuhan University) for providing plasmids and cells. We thank B.-L. Song and J. Wang for helpful discussion. We also thank the staff at the Tsinghua University Branch of the National Protein Science Facility (Beijing) for technical support on the cryo-EM and high-performance computation platforms. Funding: This work was supported by the National Basic Research Program to S.-F.S. (2017YFA0504600 and 2016YFA0501101) and by the National Natural Science Foundation of China (91954118 to S.S., 31861143048 to S.-F.S., 31670745 to S.-F.S., and 31670746 to S.S.). Author contributions: S.-F.S. supervised the project. M.H. and Y.H. prepared the samples and performed the biochemical and cellular analyses. Y.H. and F.Y. collected the EM data. F.Y. and S.S. performed the EM analysis and the initial model building. S.S., X.Y., and D.L. performed the model building and the structure refinement, M.H., Y.H., F.Y., S.S., and S.-F.S. analyzed the structure. M.H., Y.H., and F.Y. wrote the initial draft. S.S. and S.-F.S. edited the manuscript. Competing interests: The authors declare that they have no competing interests. Data and materials availability: Atomic coordinates and EM density maps of FL-hNPC1L1-Apo (PDB: 7DF8; EMDB: EMD-30662), ΔN-hNPC1L1-Apo (EMDB: EMD-30667), ΔN-hNPC1L1-CLR-EZE (PDB: 7DFZ; EMDB: EMD-30668), and  $\Delta$ N-hNPC1L1-CLR (PDB: 7DFW; EMDB: EMD-30666) have been deposited in the Protein Data Bank (www.rcsb.org) and the Electron Microscopy Data Bank (www.ebi.ac.uk/ pdbe/emdb/), respectively. All other data needed to evaluate the conclusions in the paper are present in the paper and/or the Supplementary Materials. The plasmids for expressing human NPC1L1 protein and its mutants used in this paper can be provided by S.-F.S.'s pending scientific review and a completed material transfer agreement. Requests for the plasmids should be submitted to suisf@mail.tsinghua.edu.cn.

Submitted 24 December 2020 Accepted 3 June 2021 Published 16 July 2021 10.1126/sciadv.abg3188

Citation: M. Hu, F. Yang, Y. Huang, X. You, D. Liu, S. Sun, S.-F. Sui, Structural insights into the mechanism of human NPC1L1-mediated cholesterol uptake. *Sci. Adv.* **7**, eabg3188 (2021).